The 10 MeV LINAC

de Wijs, M.C.J.

Award date:
1995

Eindhoven University of Technology
Department of Applied Physics
Group Particle Physics
Accelerator Physics Group

The 10 MeV LINAC

By: M.C.J. de Wijs

August 1995 VDF/NK 95-xx

Report on a graduate study.
September 1994-August 1995
Guidance: Ir. R.W. de Leeuw
dr.ir. C.J. Timmermans
dr.J.I.M. Botman
prof.dr.ir. H.L. Hagedoorn

Summary

At the Eindhoven University of Technology, the electron storage ring EUTERPE is under construction. The injector chain of the ring consists of a 10 MeV 'old' medical traveling wave LINAC followed by the 10-75 MeV Racetrack Microtron Eindhoven. In this graduation report various measurements at and simulations of the LINAC are presented.

To be able to simulate the beam dynamical behaviour of the LINAC accurately, the electric and magnetic fields have to be known. The focusing electric fields of the solenoids are measured and described with a series of single loop coils. The shape of the accelerating electric field is calculated in the form of a Fourier series expansion with the computer code Superfish. The amplitude of the electric accelerating field is calculated by numerically solving the power diffusion equation for the entire accelerator.

The data obtained this way are consistent with the data supplied by the manufacturer of the LINAC. By solving the power diffusion calculation the load-line of the LINAC can be determined. This calculated load-line compares very well with the measured load-line.

Also the radius and energy spread of the outcoming electron beam have been measured. This compares quite well with the values calculated with computer code Pamela.

Contents

1 The accelerator injection chain of the electron storage ring EUTERPE

A general outline of the EUTERPE project and the accelerator injection chain of the ring is presented in some detail. This injection chain consists of a 10 MeV linear traveling wave accelerator connected by a racetrack microtron. The layout of the linear accelerator will be presented and the operation of the machine will be briefly described.

1.1 The electron storage ring EUTERPE

EUTERPE (**E**indhoven **U**niversity of **TE**chnology **R**ing for **P**rotons and **E**lectrons) is a university funded project for the realization of a small storage ring [BOT89]. In the mid-eighties the project was started as a post accelerator for the 3 MeV proton cyclotron ILEC (Isochronous Low Energy Cyclotron) [HEY89]. The ring would be used explicitly for beam dynamic studies. Soon, it was realized that the equivalent electron energy in the suggested proton ring was sufficiently high for experiments and applications using synchrotron radiation, which would allow extension of the analyses activities in the Cyclotron building. Nowadays the objective of acceleration of protons has become subordinate to the promising possibilities for an electron storage ring.

The purpose of the electron storage ring is threefold. Firstly synchrotron radiation will be generated. Secondly beam dynamic studies with and without the so-called insertion devices will be performed in order to create possibilities of fundamental studies. Thirdly the ring will be used for the education of students in the field of accelerator physics. Studies on design, experiments and theory on orbit dynamics, magnets and radio frequency (RF) systems for accelerators, data-acquisition, system controls, etc. are for a large part carried out by students.

For the generation of synchrotron radiation the project has been devided into two phases. In the first phase the synchrotron radiation in the IR, VR, UV and XUV range will be provided from the regular dipole magnets. In the second phase a wiggler magnet and various undulators (insertion devices) will be used. Synchrotron radiation in the soft X-ray region with a bright, quasimonochromatic photon beam will be provided. The synchrotron radiation generated in the ring can be used for studies in photochemistry, biophysics, surface and condensed matter science, moleculair and atomic physics.

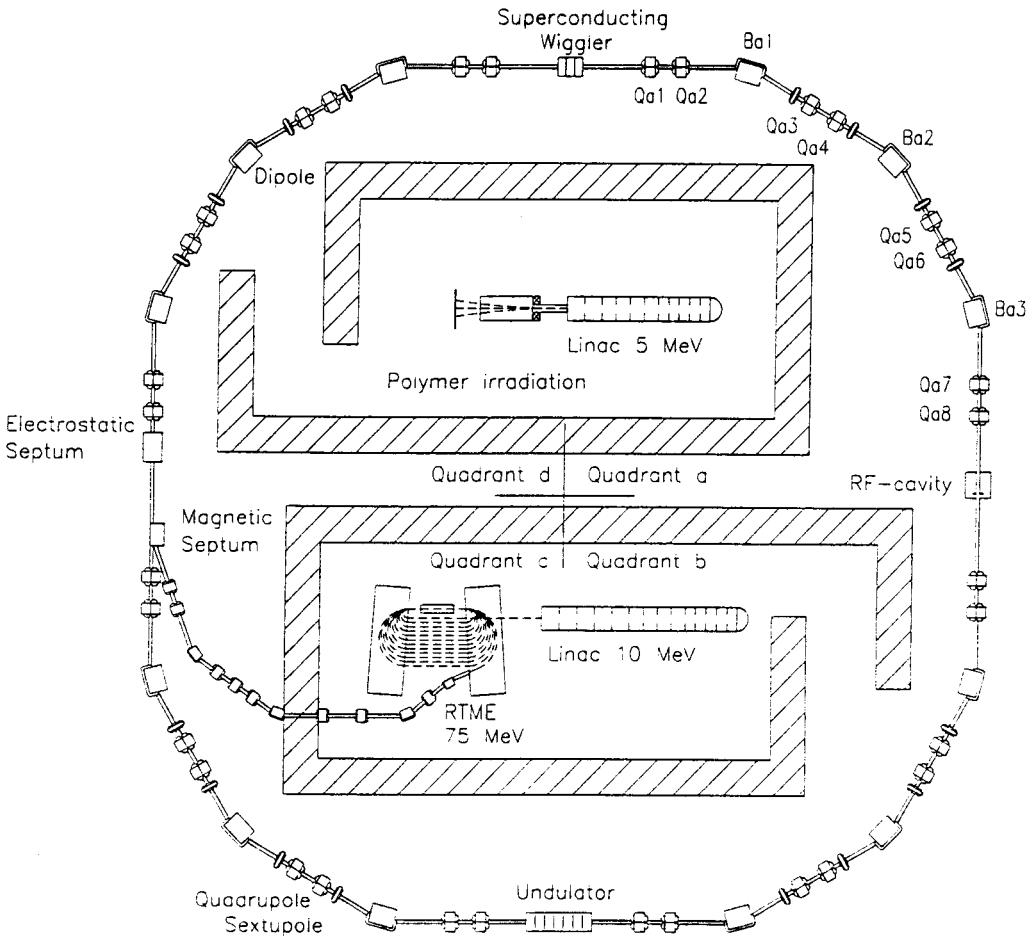

Figure 1.1 Lay out of the 400 MeV EUTERPE Ring

EUTERPE, figure 1.1, will have a circumference of 40 meter and will be located in the existing experiment hall of the Cyclotron Laboratory at the Eindhoven University of Technology (EUT). The ring is designed to store electrons at an energy of 400 MeV and a beam current of 200 mA. The beam guiding system consists of 12 dipole magnets, 32 quadrupole magnets and 16 sextupole magnets. The 12 dipole magnets will provide the synchrotron radiation. The energy loss of 2.3 keV/turn of the electrons at 400 MeV, due to this synchrotron radiation will be compensated for by a 45 megahertz (MHz) cavity, which also accelerates the electrons from the injection energy of 75 MeV to the final energy of 400 MeV [WEB94].

1.2 The accelerator injection chain

EUTERPE will be injected from an accelerator injection chain that consists of a 10 MeV traveling wave linear accelerator (LINAC) followed by a 10 - 75 MeV racetrack microtron. Since the two accelerators have to operate synchronously, a number of parameters of both machines have to be closely related. Especially phase and frequency

of both magnetrons that power the two accelerating structures have to be controlled carefully.

1.2.1 The linear accelerator

The 10 MeV traveling wave linear accelerator is an 'old' medical LINAC. At the Catherina hospital in Eindhoven it was used for cancer treatment by means of X-ray and electron therapy. After the machine was written off, it was donated to the EUT. The LINAC has been completely revised and is suitable for electron beam manipulation.

Table 1.1: Parameters of the LINAC

length	2.255
average gradient(MV/m)	4.4
electron energy (MeV)	10.0
FWHM energy spread.(%)	5
macro pulse current (mA)	30
operating frequency (MHz)	2998.3
pulse repetition rate (Hz)	50, 150, 300
pulse duration (μs)	2.2
filling time (μs)	0.45
transverse emittance (mm-mrad)	?

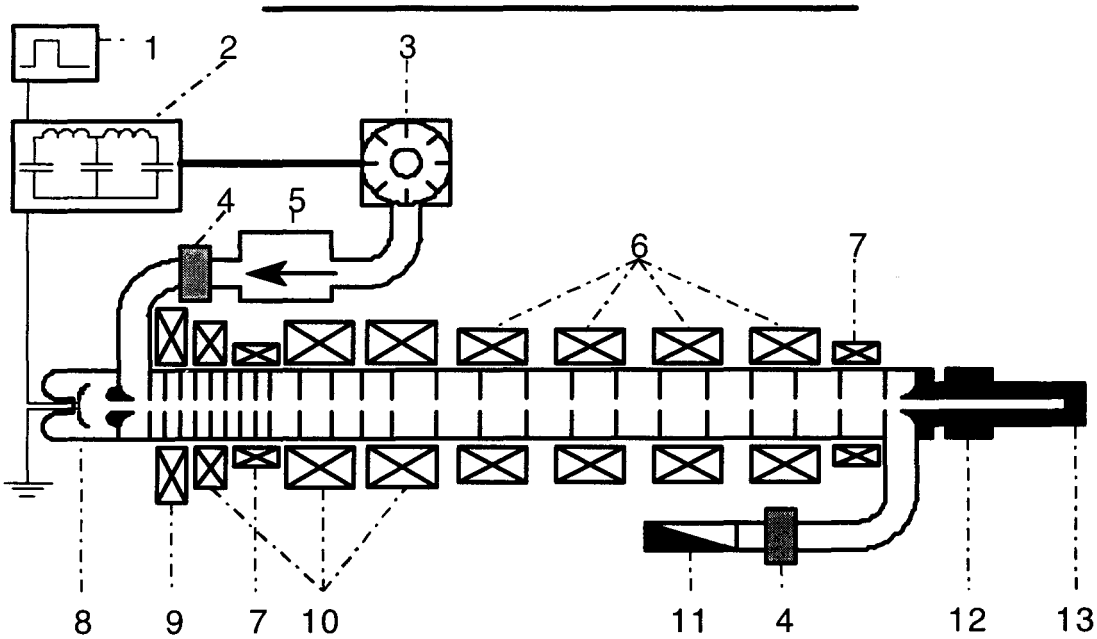

Figure 1.2 Schematic lay out of the 10 MeV LINAC.
1) Pulse generator (PRF). 2) Pulse shaping network. 3) Magnetron. 4) Vacuum window. 5) Isolator. 6) Last 4 solenoids. 7) First steering coil. 8) Electron gun. 9) First solenoid. 10) Second 3 solenoids. 11) RF dump. 12) Isolator ring. 13) Faraday cup.

The key components of the LINAC are depicted in figure 1.2. The high power RF pulse generated by the magnetron is coupled into the disk loaded traveling waveguide via a mode transformer. Once the electrons, generated in the gun by a high tension pulse, enter the waveguide they are accelerated by the electromagnetic wave.. At the end of the LINAC the remaining of the EM wave is separated from the electrons via a second mode transformer and is dumped into a load. The principle of acceleration will be explained in more detail in paragraph 1.3.

1.2.2 The racetrack microtron

The racetrack microtron is a compact recirculating type of bunched electron beam accelerator. Its main components are two 180 degree bending magnets and a resonant type of accelerating structure or cavity. Due to the recirculating nature of the racetrack microtron, the electrons, at their passage through the machine, remain captured in bunches with a length much smaller than the wavelength of the cavity. This principle of phase stability in the cavity provides a stable sharply pulsed output beam with small relative energy spread.

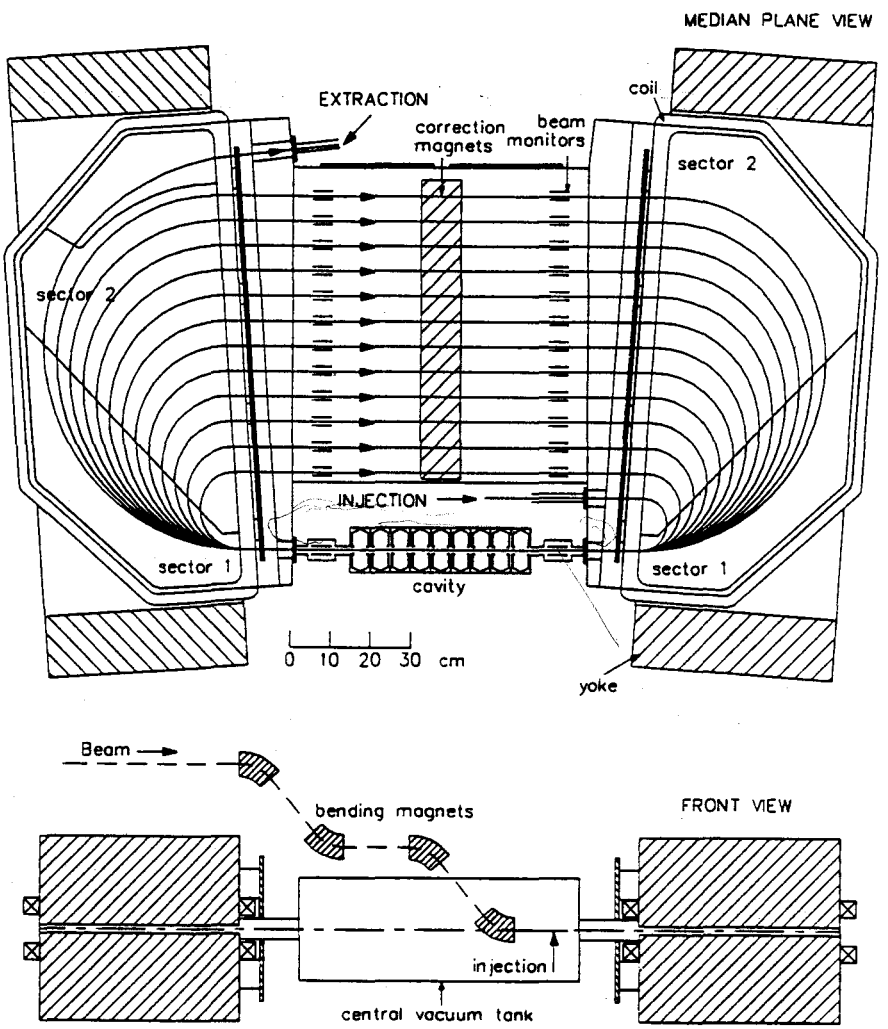

Figure 1.3. The racetrack microtron, with courtesy of G.A. Webers.

Figure 1.3 depicts the schematic layout of the Eindhoven Racetrack Microtron. The electron beam from the LINAC is injected at an energy of approximately 10 MeV. After the first bend in the right-hand bending magnet the electrons pass the cavity for the first time. During this passage their kinetic energy is raised by 5 MeV. The accelerating structure of the racetrack microtron Eindhoven is a 17-cell bi-periodic standing wave on-axis coupled cavity made out of copper. It consists of 9 capacitively loaded accelerating cells coupled by 8 flat pancake-like coupling cells. The structure operates at a resonant frequency, f_0 of 2998 MHz in the $\pi/2$-mode and provides the mentioned energy gain of 5 MeV each passage [COP94].

Due to the higher energy the first bending radius in the left-hand bending magnet is larger and the particles enter the mid vacuum chamber. In this mid vacuum chamber the position of the individual orbits is measured and corrected [THE94]. The electrons are bend again in the right-hand bending magnet, and so on.

For optimized focusing properties the bending magnets of the racetrack microtron Eindhoven contain two distinct sectors with different magnetic field strengths and reversed field clamps. This kind of magnet provides focusing forces at three edges: at the entrance of the magnet, at the exit of the magnet and at the transition of the sector boundary. In order to obtain closed orbits each of the bending magnets have to be rotated by 4.5^0 in their median planes.

After 13 passages through the cavity and a total energy gain of 65 MeV the electron beam is extracted. In order to facilitate extraction of the electrons, the field profile for the last bend has been altered from a two sector profile into a three sector profile, which lowers the bending angle by approximately 6^0, sufficient for easy extraction.

1.2.3 Radio frequency high power set up

The accelerating structures of both the linear accelerator and the racetrack microtron are powered individually by a high power magnetron. The RF power generated by the identical magnetrons is partly dissipated in the accelerating structures, the rest of the power is used for acceleration of the electrons.

Since the electron bunches, that are formed and accelerated in the linear accelerator, had to be accelerated further on in the racetrack microtron at a well defined synchronous phase there has to be a defined frequency and phase relation between both magnetrons. They not only have to oscillate at the same frequency, but moreover, the phase difference has to be kept constant. Because the magnetron is a free running oscillator, not an amplifier, this relation has to be obtained at the high power level.

This frequency and phase relation will be assured by feeding part of the power (-7 dB) from the magnetron with the longer pulse duration, i.e. the magnetron that powers the accelerating structure of the racetrack microtron, into the other magnetron that powers the LINAC. By injecting this power before the second magnetron is triggered, this magnetron is forced to lock onto this pre-injected frequency and phase [LEE96].

1.2.4 Electron Beam transport lines

Two transport lines provide the electron beam transport between the three accelerators. The first transport line guides the electron beam from the linear accelerator to the injection spot of the racetrack microtron (figure 1.4). This transport

line not only guides the beam from one machine to the other, but also matches the six dimensional emittance of the linear accelerator to acceptance of the microtron. The total beam transport line consist of a quadrupole triplet followed by a bending section and a quadrupole doublet. The entire length is about 2 m [LEE94].

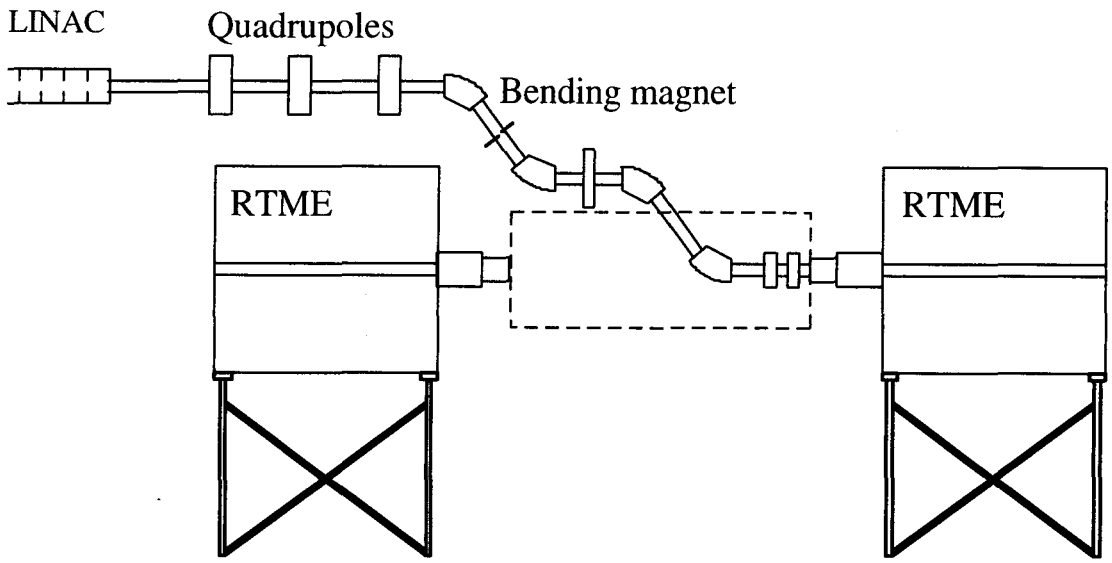

Figure 1.4 The beam transport line between LINAC and RTME

The second transport line guides the beam from the extraction spot of the racetrack microtron to the injection spot of EUTERPE. Since the longitudinal acceptance of the ring is large, the transport line only matches the 4-dimensional transverse emittance of the racetrack microtron beam to the transverse acceptance of the ring. The transport line consists of two doubly achromatic bending sections and two quadrupole doublets [LEE94].

1.3 The 10 MeV linear accelerator.

As stated before the 10 MeV linear accelerator LINAC will be used as pre-accelerator for the Racetrack Microtron Eindhoven (RTME). In this section the principle of acceleration of the LINAC will be explained and a description of the layout of the machine in its present state will be given.

In a linear electron travelling wave accelerator (LINAC), the electrons are accelerated by interaction with a travelling electromagnetic wave. The part of the electromagnetic (EM) wave that accelerates the electrons is the axial component of the electric field, $E_z(r)$, where r is the distance to the optical axis.
In a cylindrical waveguide several modes of electromagnetic waves can exist. Generally they are known as Trans. Electric (TE) and Trans. Magnetic (TM) modes. The first one is not suited for acceleration, since it has no axial component of the electric field, but the TM modes do have an axial component of the electric field. The TM mode that is used to accelerate electrons is the TM_{01} mode and has maximal electric and minimal magnetic field on the axis.

In a cylinder the mode with the lowest cut-off frequency is the TE_{11} mode, followed by the TM_{01} mode, see figure 1.5, and 1.6. By applying the proper drive

frequency (about 3 GHz in our case) this mode is the one that is excitated. The TM_{01} can be envisioned by an axial electric field that is maximal at the axis and zero at the boundary. See figure 1.6. The fringe radial electric fields of the wave are not of importance for acceleration. The magnetic field is zero at the axis and maximal at the boundary and circulates round the axial electric field lines.

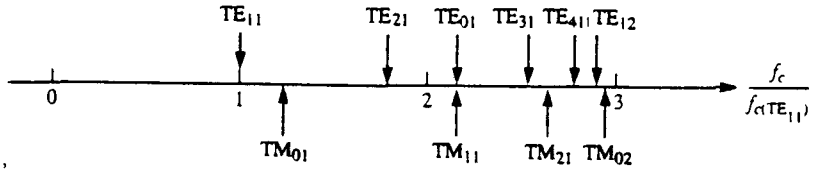

Figure 1.5 The bandpass of a cylindrical waveguide, normalised at the TE_{11} frequency.

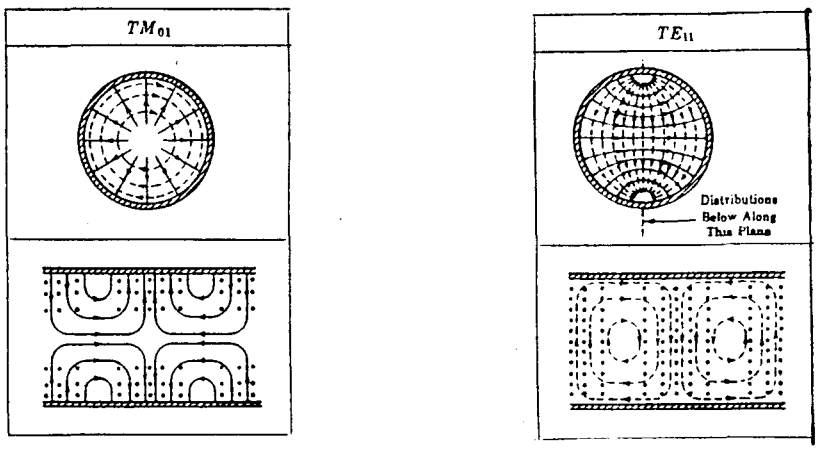

Figure 1.6. The TM_{01} mode (left) and the TE_{11} mode (right) [POZ93].

The phase velocity v_p of the EM wave should be equal to the electron velocity for optimal energy transfer from the wave to the electrons. However, v_p is larger than the speed of light c in a hollow cylindrical conductor [POZ93]. In order to slow down the phase velocity of the wave to the speed of the electrons, the accelerator tube is adapted by inserting disks with circular irises at certain distances, figure 1.7. By changing the aperture size of the irises and the distance between the irises the phase velocity can be slowed down to any desired velocity.

The disks also influence the shape of the TM_{01} mode. The electric field lines have a radial component that increases near the aperture of the disks. For the EM fields in this capacitive disk loaded cylindrical wave guide analytical approaches and numerical solutions exist. Most techniques are based on expansion of the distorted TM_{01} mode in Fourier series under the assumption that the disks are infinitely thin [LAP70]. This will be further explained in chapter 3.

The lowest Fourier mode of the expansion in the Fourier series is responsible for the acceleration of the electrons and is also the fastest. In longitudinal direction the electrons hardly notice the higher order modes. Since the electrons are accelerated on the crest of the wave, the first mode is experienced as a static field. The other modes are Lorentz transformed to the same frame of reference and are experienced as high frequency oscillations which will average to zero.

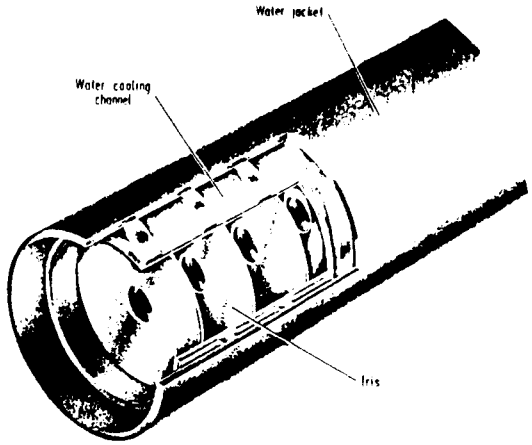

Figure 1.7 A disk-loaded cylindrical waveguide [BAT94].

The EM wave is generated by applying the high voltage (HT) pulse to a magnetron oscillator. The generated RF wave is transported down a rectangular waveguide and coupled into the circular accelerator waveguide via a door knob coupler.

The electrons are generated by applying the same high voltage pulse to an electron gun. The gun consists of a spiralled cathode, which is heated by a DC current of at least 6.0 Amperes. Before the HT pulse is applied to the gun, the gun is pre-heated for about 5 minutes, this to prevent current changes during operation. The spiralled cathode is placed in a short circular shaped tube with expanding radius, with in front the nose cone of the anode around the extraction channel. This disk shapes the field lines once the HT pulse is applied. The emitted electrons are accelerated towards the anode at ground potential and extracted through the extraction channel in the anode. After that they are launched into the disk loaded wave guide where they are accelerated by the EM wave. For the LINAC the high tension pulse is about -45 kV. This implies that the electrons have a velocity equal to 39% of the speed of light when injected into the LINAC.

The High Tension (HT) power necessary for the magnetron and the electron gun is generated in the power module. The HT part of the modulator consists of a transformer from 380 V~ to 8 kV~ and a pulse forming network. The pulse coming from the network is rectified by a number of diodes. A final transformer changes this 8 kV pulse to a -45 kV pulse. This high tension pulse is delivered simultaneous to the magnetron and to the gun. The High Tension circuit is controlled and powered by a Low Tension part (LT). This subsystem delivers the 380 V to the HT circuit. It also feeds the several parts of the HT circuit individually. The HT and the LT parts together are referred to as the modulator. The pulse forming network is triggered by a thyratron, which in its turn is triggered by a pulse from the Pulse Repetition Frequency (PRF) generator.

From the former text it is clear that during the pulse there is a continuos generation of electrons that are injected into the radio frequency (RF) structure or accelerating waveguide. So the electrons all have a different phase on the electromagnetic wave. Initially only half of the electrons are accelerated (see figure 1.5), because only half the period the electric potential is positive. The other half is de-accelerated, because it experiences a negative potential.

By a proper choice of geometry (E_z and v_p, if only the first Fourier mode of the TM_{01} wave is considered) and injection energy it is possible to catch more than half the electrons for acceleration purposes. Due to the variable E_z over the wave the electrons will be longitudinally focused in a small bunch ahead of the crest of the wave. This bunch is caught within the so-called bucket, the area of the wave where stable operation is possible. In the centre of this bucket there is an optimum phase φ_s in which the electrons move

perfectly synchronous with the wave. In the bucket the electrons oscillate around the optimum phase φ_s. The electrons in front of the optimum phase experience a smaller electric field and gain less energy, so they fall back. If they are behind the optimum phase they experience a stronger E_z and are forced back. This process causes longitudinal stability for the electrons in the bucket. For proper acceleration the phase velocity v_p is increased simultaneously with the electron velocity v_e by varying the geometry of the waveguide, until v_e is approximately equal to the speed of light c and then the geometry is kept constant.

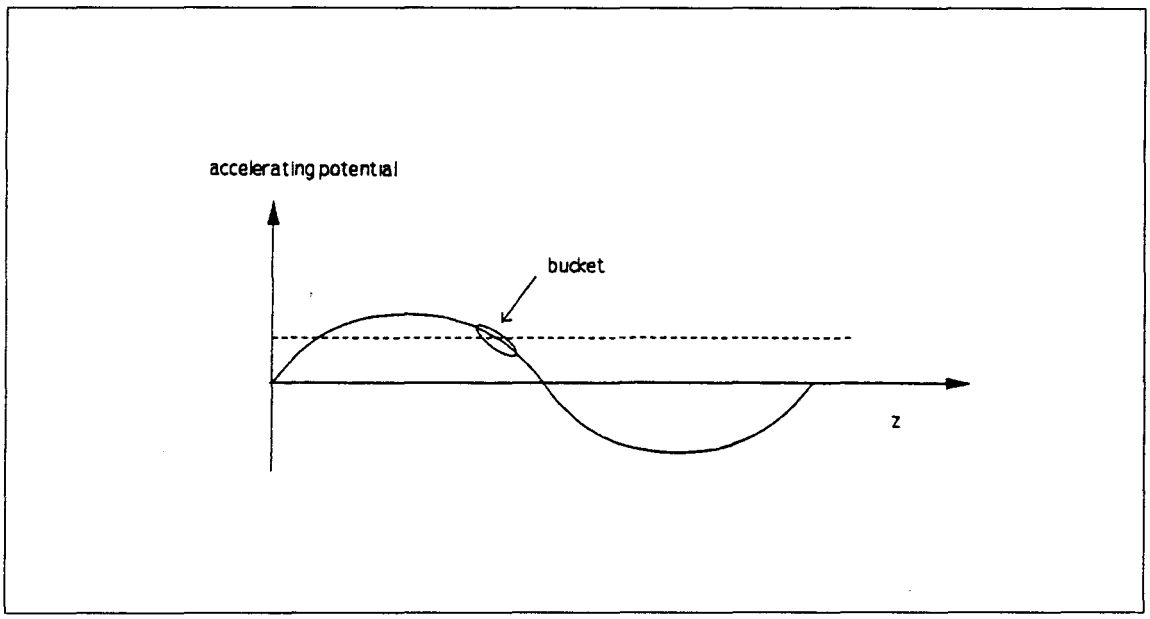

Figure 1.8. The accelerating wave (going from the left to the right) with the optimal potential marked as a dotted line.

The longitudinal stability of the electrons is the reason for inherent instability in the transverse plane [LAP70]. To compensate for this instability, solenoids are used along the accelerator tube. These solenoids have a continuously radial focusing effect, their working will be explained in chapter 2. The LINAC has a total of 8 solenoids devided in 3 groups. In practice it could be necessary to centre the beam additionally due to background magnetic fields. This is done with horizontal and vertical steering dipoles at the begin and end of the accelerator.

1.4 Control and safeguarding of the 10 MeV LINAC

The 10 MeV LINAC has several subsystems that are necessary for the operation of the machine. All these systems had to controlled and safeguarded for proper operation of the LINAC. In this section the control and safeguarding system will be discussed.

The control of the LINAC is done with a Phydas system built around a M68030 processor, whereas the safeguarding is done with a Siemens Programmable Logic Controller (PLC).

The Phydas system controls the power supplies of the different bending and focusing magnets. These are set by writing a value to the appropriate DAC's in an analog bus. This value is used as set point for a the appropriate hardware stabilisation circuit, that controls the output current of the power supplies. Also the heating current of the electron

gun of the LINAC 10 and the magnetron frequency are set by a single write statement. The trigger pulse repetition circuit is set by writing the appropriate value to the trigger pulse frequency (PRF) generator on a foundation unit in the Phybus. These external circuits have the great advantage that the Phydas system is not occupied with regulating tasks during operation of the accelerators, so that it can be suited for data-acquisition at the different experiments instead. For a description of a general Phydas system, see [MUT95], and more for this specific configuration [GRA95].

The Programmable Logic Controller PLC is used to put the different parts of the accelerator into operation in a predefined sequence and is also used for safeguarding. For a complex machine as an accelerator is, it is important to make sure that it is not possible to damage the machine by improper handling of the operator. Often a number of conditions have to be fulfilled before a certain part of the machine, for example the electron gun, can be put into operation. The gun has to be pre-heated and the current must be limited. The current limits of the focusing and steering coils, the water flow of the different cooling systems, the pressure vacuum systems of the LINAC are all controlled by the PLC. Also the PRF generator can be blocked by a PRF inhibit signal from the PLC. If not all conditions for safe operation are fulfilled or in case of a fault indication, the machine or part of it is switched off. The room safeguarding is also taken care of by the PLC. The current status of accelerator, as monitored by the PLC, is displayed on the screen of a personal computer via the visualisation program INTOUCH.

By separating the control and safeguarding over a Phydas system and a PLC it is possible to obtain precise, reliable and safe operation of the complex set-up of the 10 MeV linear accelerator. Even when the project is still in its experimental phase.

1.5 The contents of this report

This report is the result of a graduate study performed at the Accelerator Physics Group at the Eindhoven University of Technology and deals with the 10 MeV injector LINAC of the electron storage ring EUTERPE. Measurements of parts of the machine: e.g. focusing and steering coils, on the beam quality and simulations of the electron beam dynamics will be presented. The purpose is to evaluate the output of the LINAC, and eventually to match these output parameters to the input parameters of the Racetrack Microtron Eindhoven.

In chapter 2 some introductory measurements at the various components of the LINAC will be described. The magnetic field measurements on the steering and focusing coils will be discussed. The HT and RF envelopes of the magnetron will be presented. Measurements on the stray magnetic fields from magnetron, isolator, ion getter pumps and the influence of the earth magnetic field and the measures that have been taken to eliminate the influence of these stray fields are described.

Chapter 3 contains the RF power and field calculations. The Fourier coefficients for the electric fields will be derived analytically and numerically. The power distribution and the accompanying electric fields along the LINAC will be presented.

In the fourth chapter electron beam dynamics of the LINAC, simulated with the computer code Parmela, will be discussed. For this simulation the electric field calculations derived in chapter 3 were used as input parameters.

In chapter 5 results of measurements on the electron beam behaviour will be discussed. The strength of the focusing and steering coils is optimized for maximum output current. The measurements on the output current as a function of the heating

current of the spiraled cathode wire, beam radius and the so-called load line of the LINAC will be presented. This will be concluded with a presentation of the emittance and energy spread measurements.

In chapter 6 concluding remarks and recommendation for further efforts will be given.

2 Measurements on subsystems of the LINAC

Before the LINAC was put into operation the individual subsystems have been tested, as a result of these tests some had to be modified. All the main subsystems: as steering and focusing coils, the HT pulse generation and the magnetron have been investigated. The influence of stray magnetic fields was eliminated before the LINAC was put into operation.

2.1 The steering coils.

In this section the steering coils are described, as well as the effect these coils have on the beam. The LINAC is supplied with four steering aircoils. These are placed as pairs at the entrance (after 34 cm) and exit (after 195 cm) of the accelerator tube, which has a total length 225 cm, figure 1.3. The first pair of coils is necessary to bend the beam to the optical axis of the accelerator waveguide. The pair of coils at the end is placed likewise and can be used to bend the beam to the optical axis of the beam transport system following the LINAC.

By applying a magnetic field $\vec{B}$ to a beam of electrons, each electron experiences the Lorentz force :

$$\vec{F}_L = -e \cdot (\vec{v} \times \vec{B}), \tag{2.1}$$

where e is the electron charge and v the velocity of the electron. The beam is bend by the magnetic field, since the Lorentz force is perpendicular to the velocity and the magnetic field.

The bending angle φ depends on three parameters: the electron impulse p, the applied magnetic field B and the interval on which the particle interacts with the magnetic field.

The impulse p is given by:

$$p = \frac{1}{c}\sqrt{T^2 + 2E_0T}, \tag{2.2}$$

where E_0 is restmass and T is the kinetic energy of the electron.

The relation between the amplitude of the magnetic field B, radius of curvature ρ, impulse and the charge is given by:

$$B\rho = \frac{p}{e}. \tag{2.3}$$

The combination of bending angles and radius of curvature is given by:

$$\varphi\rho = l, \tag{2.4}$$

with l the interaction length.

Equations (2.2), (2.3) and (2.4) can be combined to:

$$\varphi = \frac{ecBl}{\sqrt{T^2 + 2E_0T}}. \tag{2.5}$$

B and l can be determined by measurements, the kinetic energy T is estimated for by calculations with the computercode Parmela (see Chapter 4):and viz. 1.5 MeV for first pair of coils, and about 10 MeV for the second pair.

Both the horizontal (1R) and vertical (1T) magnetic field of the first pair of steering coils have been measured with a Hall probe mounted on a plastic tube, which was inserted into the accelerator wave guide. The result of the measurements is depicted in figure 2.1 and 2.2.

For a supply voltage of 8.00 V for the Hall probe the relation between the voltage V_{Hall} from the Hall-probe and the magnetic field B is given by

$$B = aV_{Hall} + b,$$

where a =200.1 (Gauss/V) and b =-798.2 (Gauss) for a magnetic field strength ≤ 400 Gauss. These values were determined with a calibration magnet.

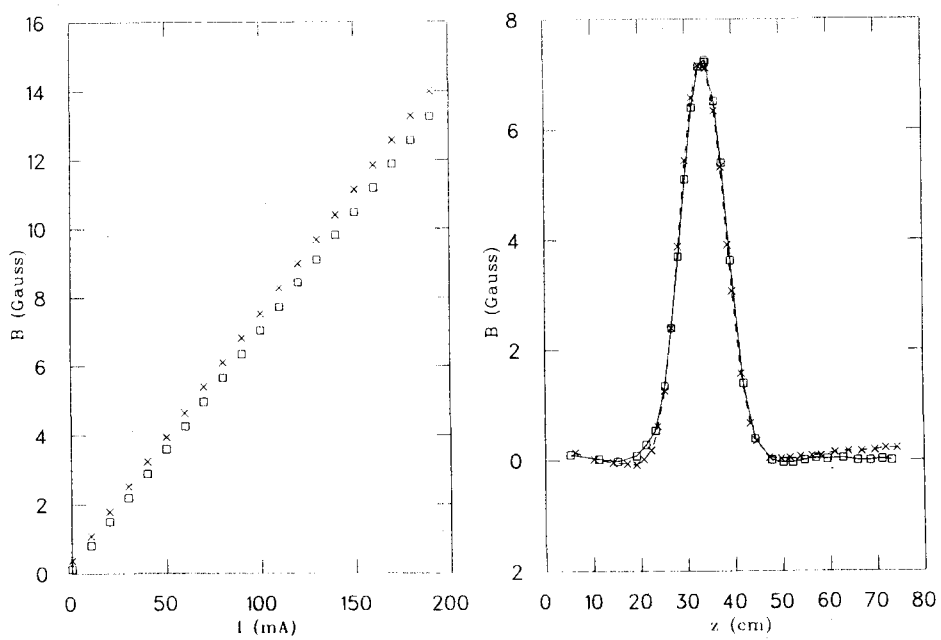

Figure 2.1. Left magnetic field as function of the current through the steering coils, right: the field profile (□ = 1R and X = 1T) for I =100 mA.

The measured field profiles of the steering coils in figure 2.1 can be replaced by a rectangular field profile [BOT88]. The field integral I_{int} of this effective field model :

$$I_{\text{int}} = \int Bdz = B_{\max} l_{eff}, \tag{2.5}$$

equals the measured field integral. With this effective field model the maximum bending angle due to these steering coils can be calculated with equation 2.5, see table 2.1 for results:

Table 2.1: *The maximum bending angle φ_{max} of the first pair dipoles.*

Coil	l (m)	max. I_{int} (Gauss.m)	T (MeV)	ϕ_{max} (mrad)
1R	0.10±0.01	1.37±0.01	1.5±0.2	22.2 ± 0.5
1T	0.10±0.01	1.37±0.01	1.5±0.2	22.2 ± 0.5

These maximum bending angle of approximated 22.2 mrad result in a maximum deviation of 50 mm with neglect of the focusing coils and accelerating fields. These 50 mm is almost five times the aperture radius of the accelerator waveguide.

The results for the second pair of steering dipoles are depicted in figure 2.2 and table 2.2 :

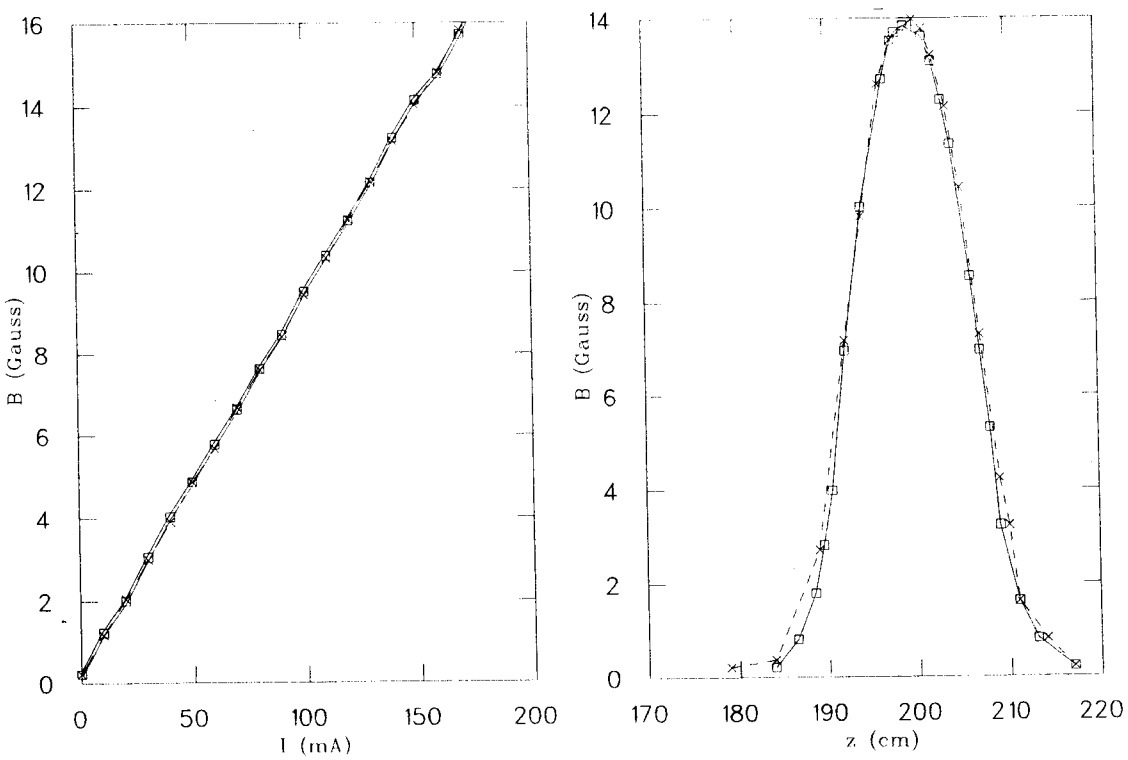

Figure 2.2. Left magnetic field as function of the current through the steering coils, right: the field profile (□ = 2R and X = 2T) for I_{exc} =150 mA.

Table 2.2: *The maximum bending angle of the second pair dipoles.*

Coil	l (m)	max I_{int} (Gauss m)	E (MeV)	ϕ_{max} (mrad)
2R	17.0±0.01	3.0±0.01	10.0±0.02	8.6± 0.5
2T	17.0±.0.01	3.0±0.01	10.0±0.02	8.6± 0.5

With these last steering aircoils the emittance angle of the beam after the LINAC can be influenced. This can be necessary to steer the beam into RTME at the correct point and angle of entrance.

2.2 Solenoids.

The LINAC is equipped with eight solenoids (see figure 1.3) in order to compensate for the inherent transverse defocusing action of the RF wave. Solenoids are often used in low energy LINACs. They are mechanically simple and focus all passing charged particles to the axis. In the middle of a long solenoid the magnetic field B near the centre only has a component $B_z(z,r)$. In the fringe field however, the magnetic field has a radial component $B_r(z,r)$ as well. If a charged particle enters the fringe field, the Lorentz force will cause the particles to rotate with a velocity v_θ around the optical axis. Due to this angular velocity v_θ and the field B_z, there will be a radial force F_r towards the axis of the solenoid:

$$F_r = e v_\theta B_z , \tag{2.6}$$

Since this force works all along the solenoid, the focusing strength $1/f$ will be proportional with the length of the solenoid l, the magnetic field B, and inverse proportional to the impulse p_0 [ ]:

$$\frac{1}{f} = \frac{1}{4}\frac{e^2 B^2 l}{p_0^2} = \frac{l}{4\rho^2} . \tag{2.7}$$

If solenoids are placed after each other they will act as one with increased focusing strength, due to the increased length l .

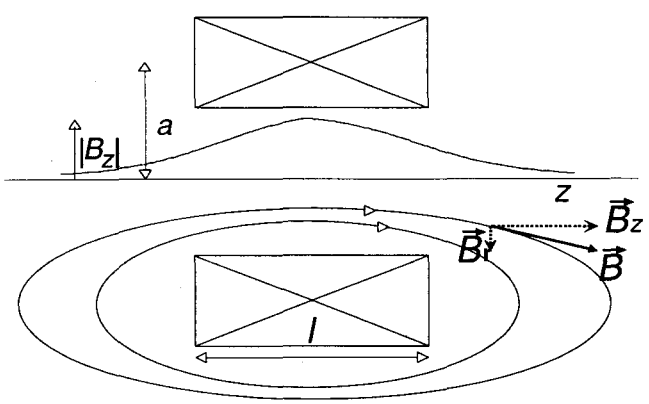

Figure 2.3 Schematic representation of a solenoid with field lines and the amplitude of the magnetic fields.

The solenoid fields are measured to be able to implement the solenoids in the simulation computer code Parmela, however Parmela only uses single loops as background fields in the accelerating process. Therefore the measured field profiles are therefore approximated by thin layer solenoids, which in turn are replaced by a number of single loop currents. These loops are then implemented in Parmela (Chapter 4) as background focusing coils. The step in between is taken to limit the number of fit parameters in each step. Since the magnetic field of the various solenoids could not be measured solenoid for solenoid, but only as a group (see figure 1.3) it is more difficult to find the correct approximation at each step.

The longitudinal magnetic fields $B_z(z,0)$ on the axis of the first two solenoids of the LINAC have been measured with the same Hall probe as in the previous section. Since the orientation of the fields is different now, the probe had to be bend over 90 degrees. If the longitudinal field is known and approximated by a continuous function, with a sixth order derivative, the off-axis and fringe fields can be approximated with the following equations [PAR94]:

$$\begin{aligned} B_z(z,r) &= B_z(z,0) - \frac{1}{4}r^2\left(B_z^{(2)}(z,0) - \frac{1}{16}r^2 B_z^{(4)}(z,0) + \frac{1}{576}r^4 B_z^{(6)}(z,0)\right) \\ B_r(z,r) &= -\frac{1}{2}r\left(B_z^{(1)}(z,0) - \frac{1}{8}r^2 B_z^{(3)}(z,0) + \frac{1}{192}r^4 B_z^{(5)}(z,0)\right) \end{aligned}, \qquad (2.8)$$

where $B_z^{(1)}$ denotes the first, $B_z^{(2)}$ the second, etc. derivative of the longitudinal magnetic field on the axis $B_z(z,0)$ with respect to z, r is the distance to the axis.

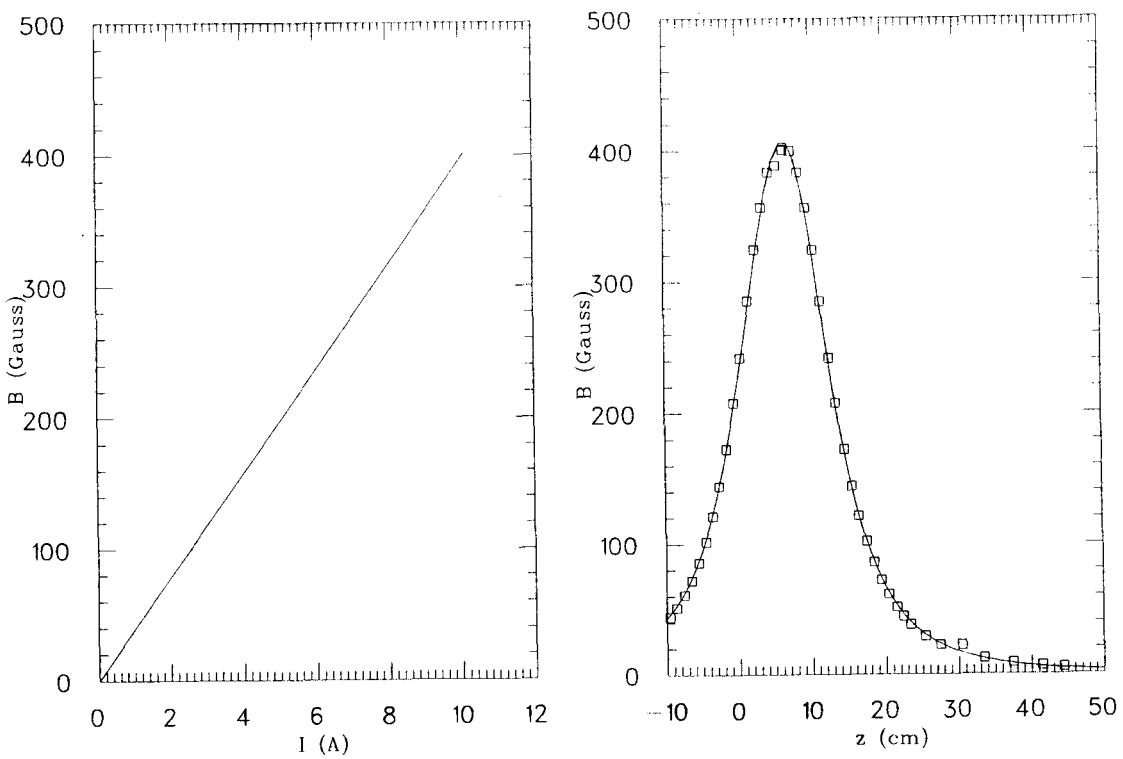

Figure 2.4 Left: The field current curve, and right: the longitudinal magnetic field of the first solenoid on axis, which are fitted by equation 2.9 and 2.10.

Figure 2.4. Depicts (as an example) the measured field profile and the B-I curve of the first solenoid. These measurements were done for all (group of) coils. These measured longitudinal profiles are fit to equation 2.9. The equation for a thin layer solenoid for the longitudinal magnetic field on axis is [JAC89]:

$$B_z(z,0) = \frac{\mu_0 NI}{2L}(\cos\beta_2 - \cos\beta_1),$$

$$\cos\beta_{2,1} = \frac{(z-z_0)\pm\frac{1}{2}L}{\sqrt{\left((z-z_0)\pm\frac{1}{2}L\right)^2 + a^2}} \quad ,\beta_2 \to +,\ \beta_1 \to - \qquad (2.9)$$

with fit parameters L the length, a the radius, N the number of coils. The current I is given and z_0 the centre of the solenoid measured from the beginning of the tube. The result of this fit is to be seen in table 2.3.

Table 2.3: *The thin layer solenoid fit parameters for equation (2.9).*

Solenoid	L (m)	a (m)	N	I (A)	z_0 (m)
1	$6.2\ 10^{-2}$	$8.5\ 10^{-2}$	746	10.0	$6.5\ 10^{-2}$
2	$7.5\ 10^{-2}$	$7.7\ 10^{-2}$	457	10.0	$15.7\ 10^{-2}$
3	$23.8\ 10^{-2}$	$7.7\ 10^{-2}$	479	10.0	$49.1\ 10^{-2}$
4	$23.8\ 10^{-2}$	$7.7\ 10^{-2}$	479	10.0	$75.2\ 10^{-2}$
5	$16.1\ 10^{-2}$	$6.86\ 10^{-2}$	346	17.5	$101.4\ 10^{-2}$
6	$16.1\ 10^{-2}$	$6.86\ 10^{-2}$	346	17.5	$123.9\ 10^{-2}$
7	$21.7\ 10^{-2}$	$7.2\ 10^{-2}$	326	17.5	$149.5\ 10^{-2}$
8	$21.7\ 10^{-2}$	$7.2\ 10^{-2}$	326	17.5	$173.5\ 10^{-2}$

The magnetic field described by equation (2.9) can be replaced by a combination of single loop coils as necessary to implement in the computer code Parmela. The question is how many coils with a longitudinal field on the axis described by [JAC89]:

$$B(z) = \frac{\mu_0 I}{2a}\frac{a^3}{\sqrt{a^2+(z-z_0)^2}^3}, \qquad (2.10)$$

are necessary to replace a thin layer solenoid and how do they have to be placed along the accelerator tube. By trying several combinations, a good solution was found by applying 7 coils per solenoid. The relative locations to the center of the solenoid are given table 2.4 for each solenoid. The single loop coils are placed as pairs at opposite sides from the centre of the solenoid, except the single loop coil in the centre. Its location is not given in table 2.4, since its relative coordinate is zero.

Table 2.4: *The single loop parameters of the solenoids of the LINAC.*

Solenoid	dz1 (m)	dz2 (m)	dz3 (m)	corr.
1	$0.46\ 10^{-2}$	$0.85\ 10^{-2}$	$3.29\ 10^{-2}$	0.250
2	$0.44\ 10^{-2}$	$1.04\ 10^{-2}$	$3.49\ 10^{-2}$	0.250
3	$3.45\ 10^{-2}$	$6.69\ 10^{-2}$	$10.39\ 10^{-2}$	0.250
4	$3.45\ 10^{-2}$	$6.69\ 10^{-2}$	$10.39\ 10^{-2}$	0.250
5	$2.36\ 10^{-2}$	$4.49\ 10^{-2}$	$7.05\ 10^{-2}$	0.250
6	$2.36\ 10^{-2}$	$4.49\ 10^{-2}$	$7.05\ 10^{-2}$	0.250
7	$3.15\ 10^{-2}$	$6.10\ 10^{-2}$	$9.48\ 10^{-2}$	0.249
8	$3.15\ 10^{-2}$	$6.10\ 10^{-2}$	$9.48\ 10^{-2}$	0.249

The current through the seven single loop coils each is one seventh of the product of *NI* of the thin layer solenoid approximation multiplied by the correction factor *corr.* given in table 2.4. The radius *a* is the same as the radius of the solenoid. The fit criteria is equal field integral (<1. 10^{-4} Gauss meter), and an absolute error of less than 0.5 Gauss with respect to the thin layer solenoid approximation.

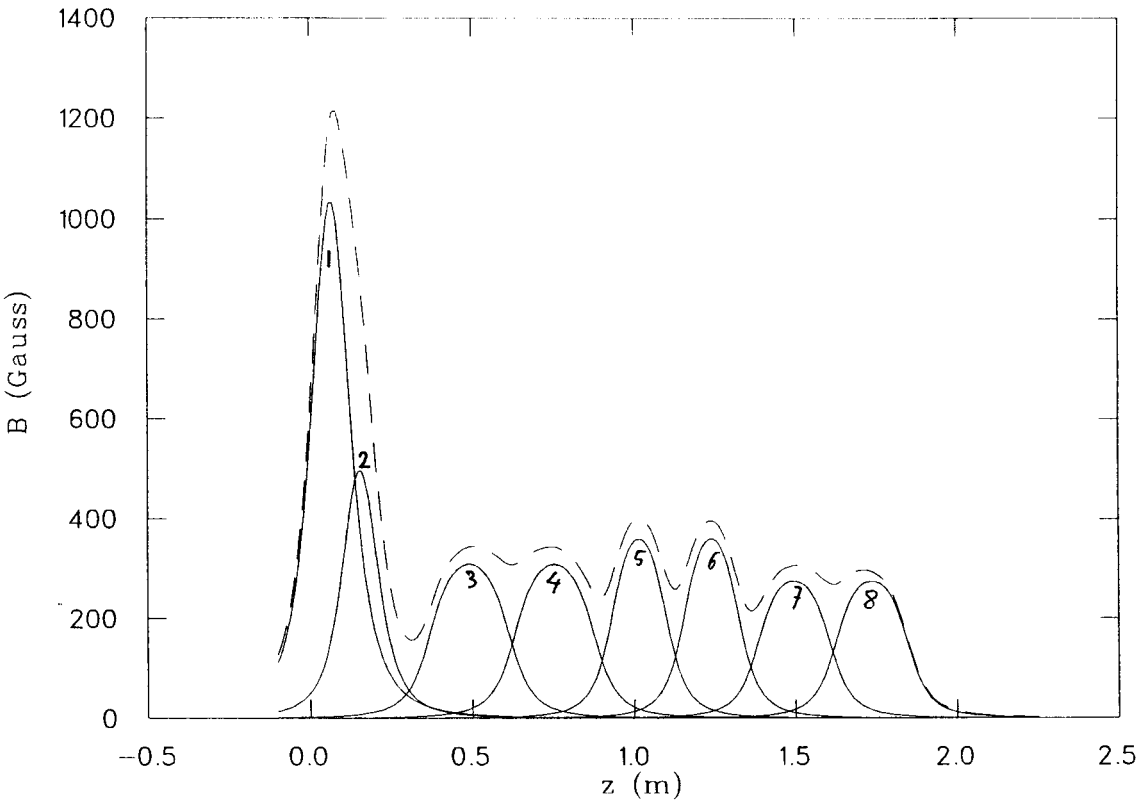

Figure 2.5 The longitudinal field of each of the solenoids. Line > thin layer and single loop coil approximation. Dashed > the total field with I_1 =20.0, I_2=14.5 and I_3= 17.5 (Amp). The subscripts denotes the groups (see figure 1.3).

2.3 The HT pulse and the magnetron

One of the important systems that has been checked, is the circuit that delivers simultaneously the HT pulse to the magnetron and electron gun. Also the envelope of the RF signal generated by the magnetron has been measured. The basic reason for these measurements was to check on the HT pulse was delivered simultaneously to magnetron and electron gun, and to check for generated RF power.

The HT pulse on the magnetron is measured with a voltage divider. This resistor-ladderwork reduces the HT voltage to a few volts, so the HT pulse can be visualized on an oscilloscope, figure 2.4. This figure also depicts the measured envelope of the RF macrostructure behind the magnetron with an inductive rand pick-up in the waveguide.

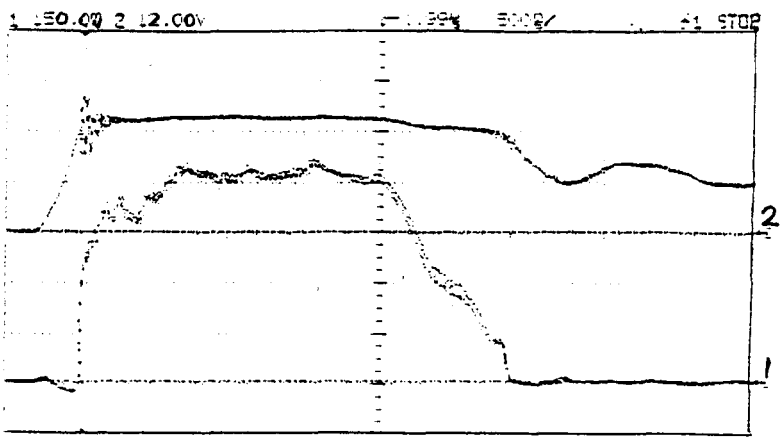

Figure 2.4 The HT pulse on the magnetron (2) and the RF macrostructure (1).

The electric pulse through the cathode wire of the electron gun is measured with the same voltage divider connected to an oscilloscope, see figure 2.5. The RF envelope behind the magnetron is displayed to have the same frame of reference, for comparison with figure 2.4

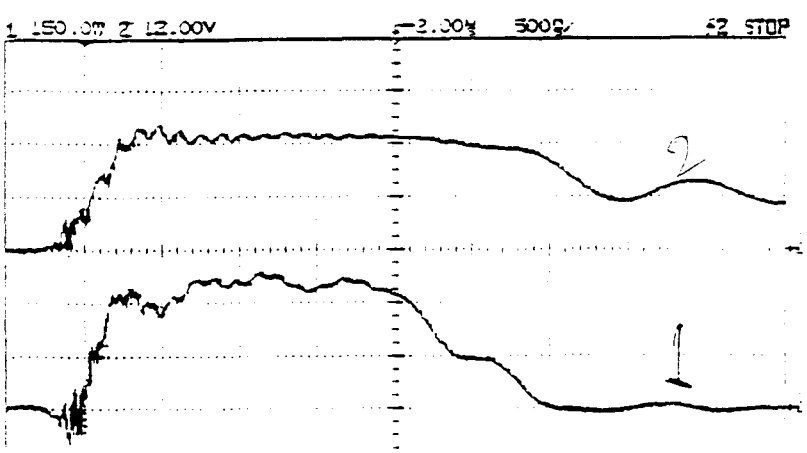

Figure 2.5 The HT pulse at the cathode of the electron gun (2) and the RF envelope behind the magnetron (1).

From figure 2.4 it can be concluded that there is a HT pulse on the magnetron and RF power behind the magnetron in the waveguide. Figure 2.5 when compared with figure 2.4 shows that the HT pulse on the cathode of the electron gun arrives at the same time as the HT pulse on the magnetron. The electron emission starts simultaneously with the incoming RF wave.

2.4 Stray magnetic fields

In this section the strong magnetic fields of the magnetron, the isolator and ion getter pomp's will be discussed. Then the earth magnetic field will be considered. The counter-measures against these magnetic fields will be presented and discussed.

The first stray magnetic field that is considered is the combined field of the magnetron and the isolator, which are placed at a distance of about 30 cm from the accelerator tube. Both the magnetron and the isolator use strong permanent magnets. The fields of these magnets are not confined to the magnetron and isolator themselves, but are also present at some distance, for example in the accelerator waveguide where they disturb the electron beam motion. This is a result of the removal of the iron housing of the LINAC, which was done to get a better access to the machine. This had as result the presence of stray fields in the accelerator tube.

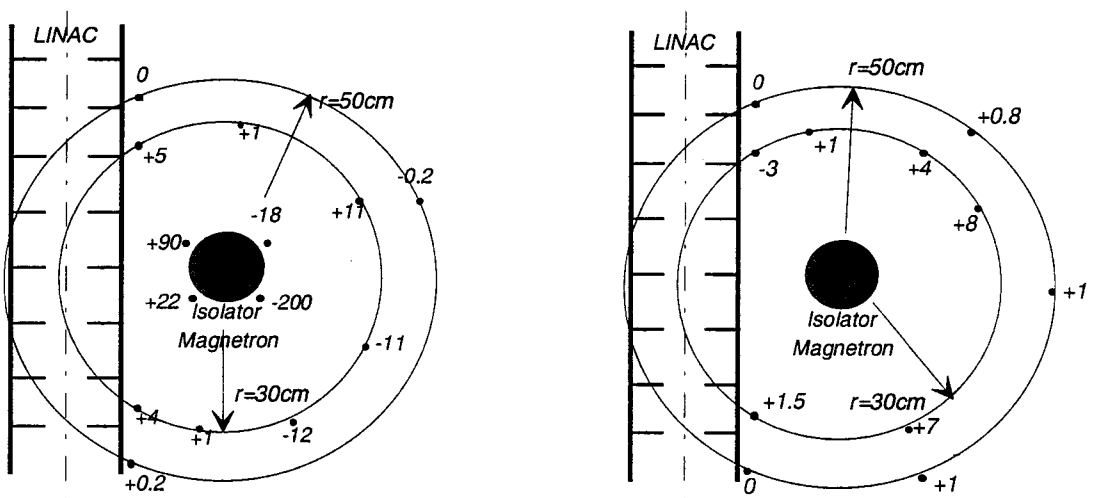

Figure 2.6 The vertical (left) magnetic stray field and the horizontal (right) stray field (Gauss) of the combination of magnetron and isolator in the horizontal plane of the waveguide.

With the Hall-probe a crude map of the vertical and horizontal magnetic fields has been made, see figure 2.6. The map shows that the maximum magnetic field in the accelerator tube is somewhere between the 12 and 90 Gauss. The field is present along 1 m of the accelerator, so the field integral is quite large. The effect of this stray field is much larger then the maximal effect of the steering dipoles, see section 2.1.

To minimize the effect of these magnetic fields the magnetron and the isolator combination was moved away to a distance of 1.2 m and further to the end of the accelerator. At a distance of 1.2 meter the stray field due to these counter-measures is zero in the accelerator, as was checked by measurements.

The parasitic field of the ion getter pumps has been measured with the Hall-probe. The field is nearly vertical and almost cylinder symmetric. The field varies from 5 Gauss at the axis of the accelerator tube to 200 Gauss directly on the gap of the ion getter pump magnet. The magnetic field is experienced by the electrons in the tube over an interval of 20 cm for each ion getter pump. To minimize the magnetic field in the accelerator tube, an enclosure of an iron cylindrical housing with a thickness of 1 cm was chosen. This solution leads to a magnetic field that is reduced by more then a factor 10. The former solution of creating distance between the tube and the magnet was not feasible due to the fixed locations of the ion getter pumps. By closing the bottom of these enclosures the magnitude of the field is even further reduced.

Finally a correction for the earth magnetic field has been made. The earth magnetic field is a constant field at the background of the whole acceleration process. In the Netherlands the magnitude of the earth magnetic field is about 0.47 Gauss and points downwards [WIN78]. The direction of the earth magnetic field is expressed in declination and inclination. The inclination is defined as the angle between the magnetic field and the horizontal plane, which is 67^0 in the Netherlands. The declination is defined as the angle between the horizontal component of B and the astronomical north and is about 3^0.

The effect of the presence of the earth magnetic field can be calculated by using the equation (2.9), which gives the deviation Δx:

$$\Delta x = \frac{cBl}{E}\left(1 - \frac{\gamma_0}{\gamma - \gamma_0}\ln\frac{\gamma}{\gamma_0}\right), \tag{2.9}$$

where γ_0 is the initial and γ the final dimensionless energy from equation (2.10)

$$\gamma = 1 + \frac{T}{E_0}, \tag{2.10}$$

in where l is the length of the accelerator tube and B the magnitude of the earth magnetic field. The equation is valid under assumption that the accelerating field E is constant [LAP70]. If the average accelerating field E is 5 MV/m (section 3.3), l is 2.25 m and γ_0 is 1 and γ is 20.6 (the electrons have a final energy of 10 MeV) the deviation due to the earth magnetic field is 5.4 mm. From this value it follows that for electrons which are accelerated on the axis in the bucket on the electromagnetic wave, get this deviation of 5.4 mm. Other electrons will not reach the end of the accelerator tube.

The LINAC is situated from west to east so the declination is negligible. Therefore it will not be considered. To compensate for the earth magnetic field two current wires were located in a plane with a angle of about 25^0 with the horizontal plane. Due to obstructions on the accelerator tube the required 23^0 was not possible. But in any way the influence of the difference of 2^0 will be a higher order effect. According to Amperes law a current produces a magnetic field at distance d from the wire. By calculating the vectorsum and minimizing the magnetic field, the current through the wires can be minimized.

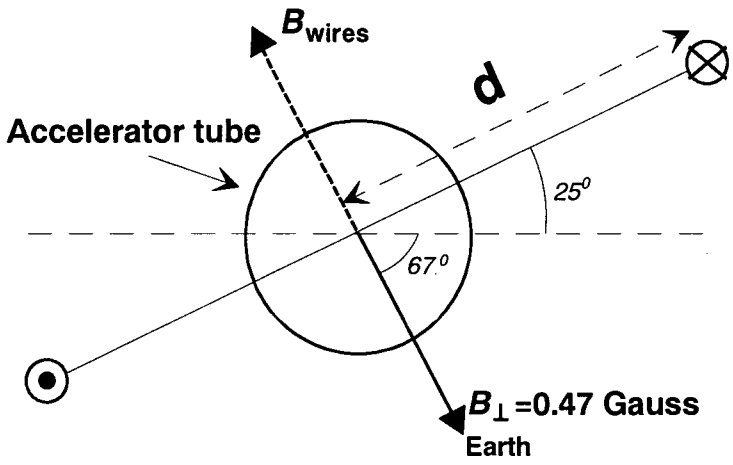

Figure 2.7. The earth magnetic field in plane perpendicular to the axis of the accelerator, with the angle of the wires.

If the residual magnetic field is measured as function of the current through the wires a minimum is found at a DC current of 11-15 Amperes, see figure 2.8. The calculated current in order to compensate the earth magnetic field of 0.47 Gauss was 16.1 Amperes. The residual vertical and horizontal magnetic field after earth magnetic field compensation are displayed in figure 2.9. The residual field has a magnitude of maximal 0.02 Gauss. The residual magnetic field is still a function of distance along the axis, this is due to the magnetization of the frame at which the LINAC is mounted and other small iron or steel parts.

When it was possible to detect the beam, see chapter 5, a measurement was done to investigate the influence of the earth magnetic field correction by measuring the macro current pulse that the LINAC generated, see figure 2.10. The measurement was done with (12 Amperes) and without earth magnetic field compensation. It is clear to see that more electrons arrive at the end of the LINAC, since the amplitude of the pulse is greater after correcting for the earth magnetic field. Also some low energetic particles arrive at the end of the LINAC, after the RF pulse, which lasts only 2.2 μs. Although these slow electrons are not accelerated by the RF wave, they gain sufficient energy from the HT pulse, which decays slower than the RF pulse, see paragraph 2.3. The energy of about 40-45 keV is sufficient to take them through the accelerator waveguide to the end of the LINAC.

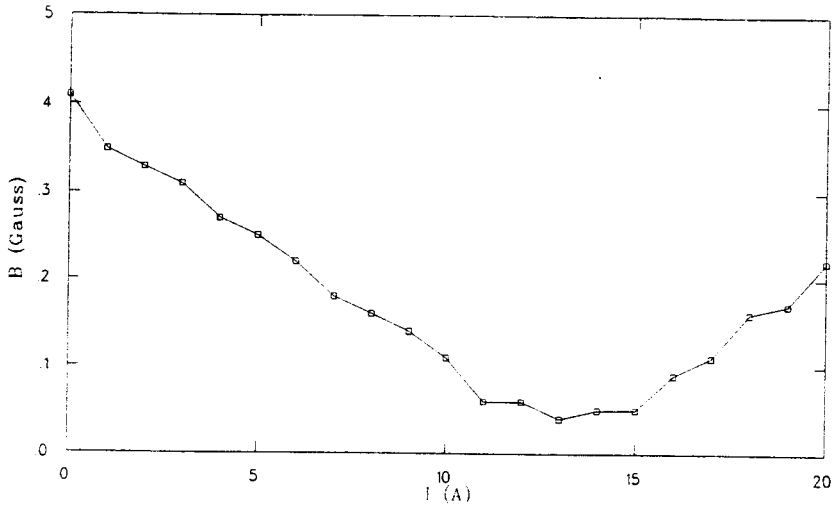

Figure 2.8 The residual magnetic field on axis of the accelerator tube as function of current through the wires on a distance of 40 cm of the beginning of the tube.

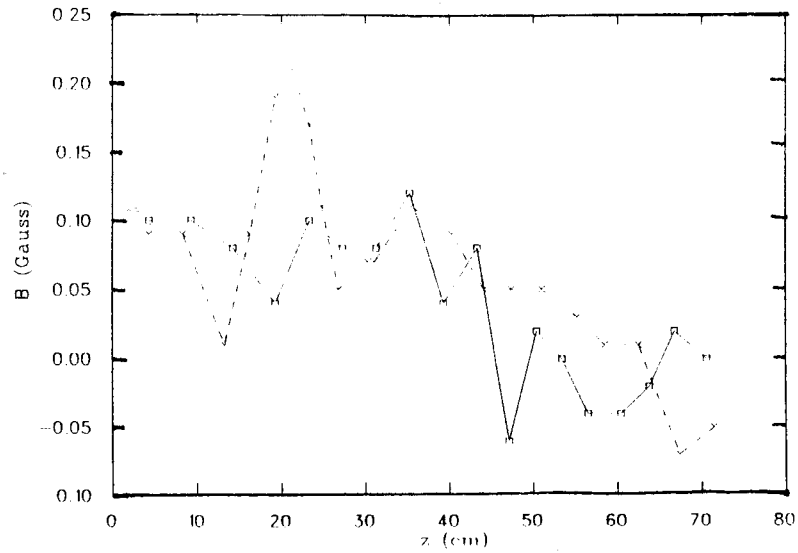

Figure 2.9. The residual vertical (continuous line) and horizontal (dashed line) fields when the earth magnetic field compensation is on

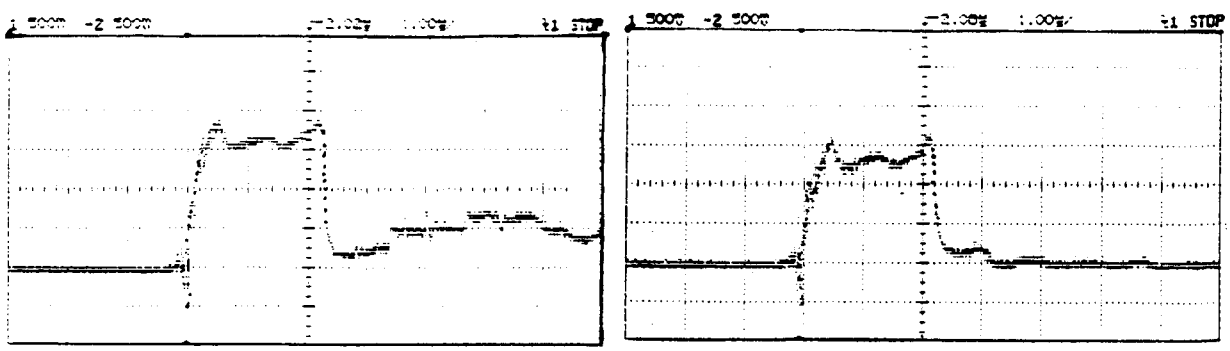

Figure 2.10 The beam with (left) and without(right) the earth magnetic field correction of 12 Amperes.

The fact that the calculated current and the measured optimized current through the wires of the earth magnetic field correction do not match, can be explained by several influences. Due to the magnetization of the frame the magnetic field can have a slightly other direction, for which there is not compensated. Another fact can be the reinforced concrete vault surrounding the LINAC and the reinforced floor of the cyclotron building, the earth magnetic field did seem to have the same direction everywhere, this is probably due to magnetization's in the iron frame of the concrete. The wires themselves do not have exactly the angle of 23 degrees, so the calculation is not totally correct, the wires have a deviation of a few degrees. So by having not been able to compensate fully for all fields, some other weak fields remain. All these effects leads in our opinion to another minimization current then the calculated one.

The conclusion is that all stray magnetic field are adequate compensated. The accelerator tube is free from weak or strong stray fields. A fact that is proven by the appearance of slow electrons at the end of the LINAC. This means that because of these slow electrons at the end of the LINAC the steering coils at the begin of the LINAC are not necessary. So for optimal beam current the first steering coils must have a current of zero and the last pair can be used to steer the outcoming beam.

3 The Electric Fields and Power modeling of the LINAC

In this chapter the form of the electric field in the individual cells is calculated with the computercode SUPERFISH and expressed in a Fourierseries. The magnitude of the electric field along the axis is calculated by numerically solving the power diffusion equation and comparison has been made with data of the manufacturer.

3.1 The form of the electric field in a disk-loaded waveguide

In a uniform circular waveguide the phase velocity v_g is always greater than the speed of light c [JAC89], however by loading the waveguide with apertured disks, the phase velocity can be lowered to any desired value.

The description of the fields in the disk-loaded waveguide is started by considering the propagation of an electromagnetic wave in a uniform cylindrical waveguide with radius a. By using Maxwell's equation in vacuum with the boundary condition that the longitudinal electric field at the boundary is zero, it can be shown that the longitudinal electric fields of the TM-modes can be written in cylindrical coordinates as [LAP70]:

$$E_z = (A\sin n\theta + B\cos n\theta)J_n(k_c\rho)e^{-jk_g z}e^{i\omega t}, \qquad (3.1)$$

where $n=0,1,..$, $k_c^2=k^2-k_g^2$ (the dispersion relation), $k=\omega/c$, k is the total wavenumber, k_c is the transverse wavenumber and k_g is the longitudinal wavenumber (figure 3.1). J_n is the n^{th} Besselfunction and A,B are arbitrary constants. By applying the boundary condition $E_z=0$ at $r=a$, it follows that $J_n(k_c a)=0$. If m is the number of times E_z is zero as r goes from zero to a, then $w_{nm}=k_c a$ is defined as the m^{th} zero of the n^{th} Besselfunction. The TM mode can be specified by n and m, so the TM modes will be referred to as TM_{nm}.

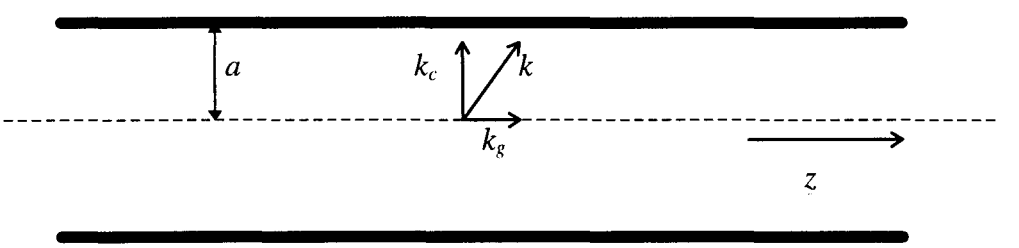

Figure 3.1. A schematic view of the k vectors of a TM mode in a cylindrical waveguide.

For the TM_{nm} mode the following dispersion relation holds (see below equation 3.1):

$$\frac{\omega^2}{c^2} - k_g^2 = \left(\frac{w_{nm}}{a}\right)^2, \tag{3.2}$$

In figure 3.2 a plot of this dispersion relation is presented. From equation (3.1)is seen that k_g^2 must be positive and real to ensure that the wave propagates without attenuation along the z-axis in positive direction. Using (3.2) the cut-off frequency is defined as $\omega_c = cw_{nm}/a$, so only waves with $\omega > \omega_c$ or $k > k_c$ can propagate without attenuation.

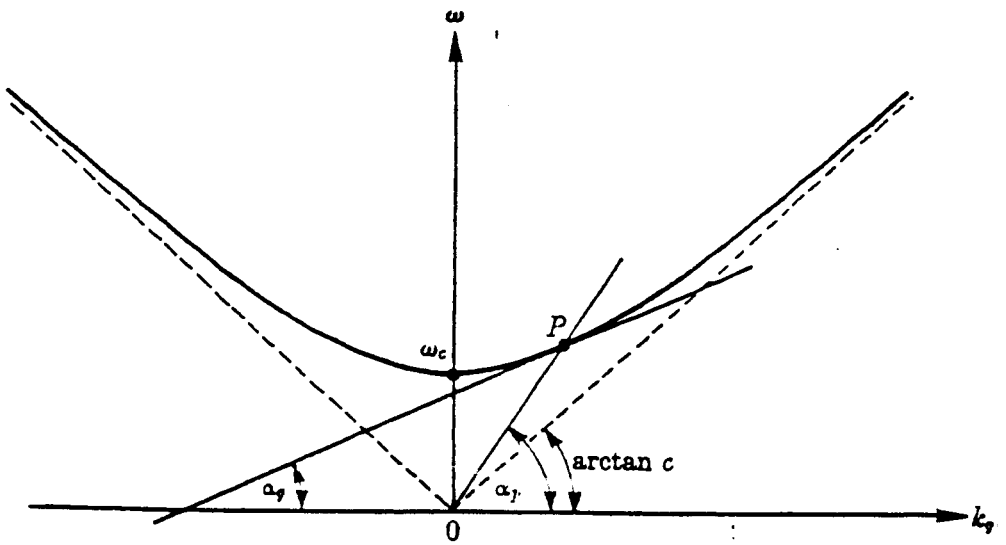

Figure 3.2: The dispersion relation for a cylindrical waveguide.

The phase and group velocity can be presented in this curve by

$$v_g = \frac{d\omega}{dk_g} = \tan\alpha_g$$
$$v_p = \frac{\omega}{k_g} = \tan\alpha_p \tag{3.3}$$

It should be noted that these are longitudinal velocities, since in radial direction the wave behaves as a standing wave. From figure 3.2 and equation (3.3) it can be deduced that $v_g < c < v_p$.

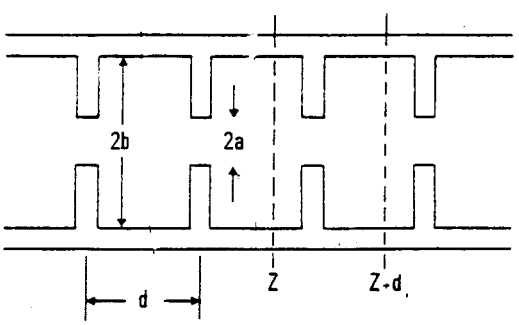

Figure 3.4 A section of a disk loaded waveguide.

To find the shape of the dispersion curve for a disk-loaded waveguide the wavelength will be assumed to be large compared with *(b-a)*, see figure 3.4. At each disk, the wave is partly reflected. However, with this assumption, this corresponds to a small perturbation of the dispersion relation. Hence, for small k_g the curve is close to the dispersion relation (3.2). The cut-off frequency for the iris loaded guide ω_{cl} can be approximated by ω_c.

As the wavelength decreases, a larger portion of the wave is reflected, due to the fact that the wave matches better the (longitudinal) geometry of the disk-loaded waveguide. The interference between incident and reflected waves will become stronger. The wave will start to deviate from the curve of the uniform waveguide. The greater *(b-a)/b*, the sooner the deviation will begin. When the wavelength of the traveling wave is equal to twice the distance between the disks, the wave will be in resonance with the structure. Now it is a purely standing wave with $v_g=0$, so the derivative of the dispersion curve must be zero, see equation 3.3. This frequency is ω_{c2}. After this point the curve will drop down to ω_{cl} again. Since we're off-resonance, and the group velocity is varying in negative direction until it is again zero at ω_{cl}. The curve will oscillate periodically with increasing k_g.

There are an infinite number of frequency intervals where propagation is possible. A more complete dispersion curve for a disk loaded waveguide is shown in figure 3.4. The frequency intervals where propagation is possible such as from ω_{cl} to ω_{c2} are called pass bands. The other intervals such as ω_{c2} to ω_{c3} , where propagation is not possible, are referred to as stop bands.

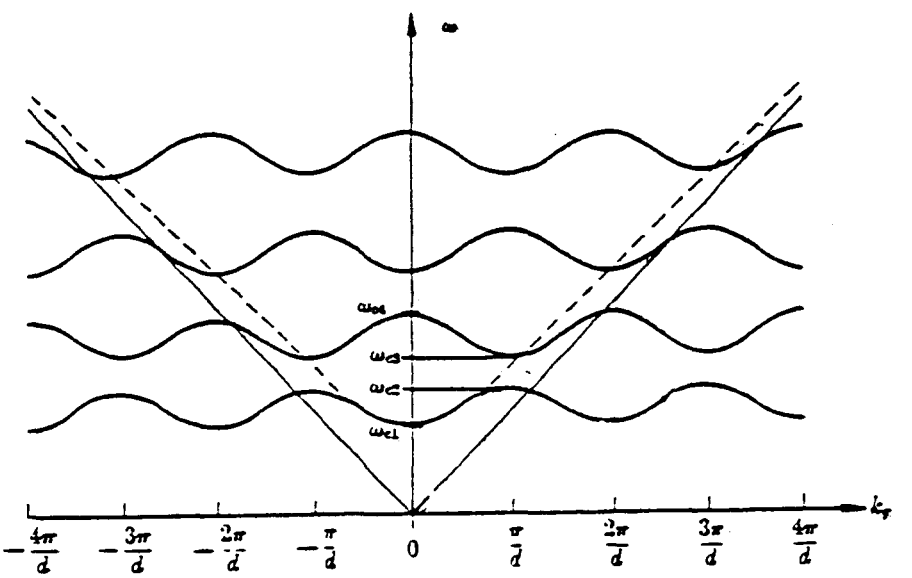

Figure 3.4 A Brillouin diagram for a circular disk loaded waveguide. The dispersion curve of the unloaded waveguide is shown as dotted curve.

Normally only the lowest TM pass-band is used. This is the TM_{01} mode. If one has a certain drive frequency ω, energy is stored in all longitudinal k_g modes (see figure 3.4, each oscillation is called a mode), with period $2\pi/d$. Most of the energy is stored in the lowest k_g mode, but some energy is stored in the other modes. Hence energy is lost, since only k_g's between 0 and π/d are used to accelerate the electrons in travelling wave LINAC's. In case of traveling wave LINAC's the $2\pi/3d$ mode often is used for acceleration. The higher k_g's are responsible for destabilization of the beam [PER68].

3.2 Fourier expansion of the axial E-field

From the previous section, one important difference between a homogenous cylindrical waveguide and the disk loaded waveguide is clear. The TM_{01} mode of the cylindrical waveguide has only one k_g for each ω, but the capacitively disk-loaded waveguide has a infinite number of k_g's at each ω. This strongly hints that the wave, especially the axial electric field can be expressed in Fourier terms based on an expansion in k_g. This shall be discussed in this section.

Before trying to calculate the Fourier coefficients of the axial electric field, it is important to know the axial fields of the TM_{01} mode in a cylindrical homogenous waveguide. Since the loading with disks is primarily intended to slow down the phase velocity, the electromagnetic fields will not be dramatically. So we will start with the fields in the homogenous cylindrical waveguide. The time dependence is given by $e^{j\omega t}$, since all calculations are time independent the time convolution will be omitted. The influence of the disk-loading will now be discussed by trying to make a Fourier expansion of the fields in a cell like figure 3.3 for r<a.

In an infinite periodic structure the wave equation must satisfy the periodic boundary condition imposed by the disks. This is obtained by choosing a solution of the form [DUF92]:

$$\begin{aligned} E(r,\theta,z) &= e^{-\gamma z}E_1(r,\theta,z) \\ H(r,\theta,z) &= e^{-\gamma z}H_1(r,\theta,z) \end{aligned}, \tag{3.2}$$

where E_1 and H_1 are periodic functions in z: $E_1(r,\theta, z+d)=E_1(r,\theta, z)$. Considering two planes in two consecutive cells, see figure 3.3, that means the fields will repeat except for the multiplication factor $e^{-\gamma d}$ which can be related to the propagation time from one cell to the next. The possibility of expressing the field in the above form is often referred to as Floquet's theorem. The original Floquet's theorem dealt with differential equations with periodic coefficients, the case of periodic boundary conditions is an extension of that work.

A periodic function, such as $E_1(r,\theta, z)$, can be expanded into an infinite Fourier series:

$$E_1(r,\theta,z) = e^{-\gamma z}\sum_{n=-\infty}^{+\infty} E_{1n}(r,\theta)e^{-j\frac{2\pi n}{d}z}. \tag{3.3}$$

For a lossless structure, γ should be imaginary, but the change of electric amplitude along the accelerator tube will be regarded in the next section:

$$\gamma = j\beta_0. \tag{3.4}$$

Hence the field becomes:

$$E(r,\theta,z) = \sum_{n=-\infty}^{+\infty} E_{1n}(r,\theta)e^{-j\beta_n z}, \tag{3.5}$$

with

$$\beta_n = \beta_0 + 2n\pi / d, \tag{3.6}$$

for a periodic structure where $\beta_0=\Psi/d$, with d the length of the cell and Ψ the operation mode of the LINAC, i.e. the phase shift per cell.

In addition the field has to satisfy the usual transverse boundary conditions of cylindrical waveguides. Thus, if one concentrates only on the lowest TM type mode, the z component of the electric field in a periodic disk-loaded structure is

$$E_z = \sum_n E_{0n} J_0(k_{c,n} r) e^{-j\beta_n z} . \tag{3.7}$$

with the more general relation

$$\beta_n^2 = k^2 - k_{c,n}^2 . \tag{3.8}$$

Notice that all space harmonics exist at a given frequency ω. Once β_0 is known all β_n 's are known. It should be remarked that the group velocity for all modes is equal [DUF92] but that each space harmonic has a different phase velocity given by:

$$v_{pn} = \frac{\omega}{\beta_0 + \dfrac{2\pi n}{d}} , \tag{3.9}$$

The coefficients can be approximated by proposing a periodical field profile [WAL48] or calculated with computer codes like Superfish, for a visualisation, see figure 3.5. These Fouriercoefficients are used in Parmela in order to describe the electric field. The amplitude of the fields are calculated in the next sections.

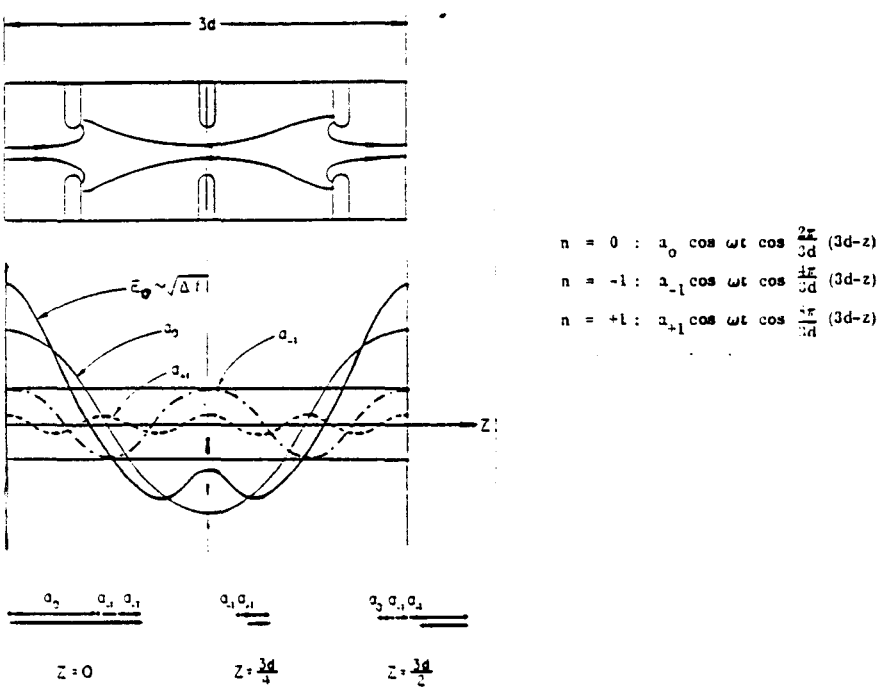

Figure 3.5 A visualisation of the electric fields described by Fouriercoefficients in a travelling wave LINAC.

3.3 Power modeling.

To calculate the power flow and the magnitude of the electric fields along the waveguide, several quantities are introduced. These quantities are structure depended and have to be calculated for each cell, unless cells are identical.

3.3.1 Shunt impedance, quality factor and filling time.

The shunt impedance R_s of an RF cavity is a figure of merit which relates the accelerating voltage to the power dissipated in the structure walls. The shunt impedance is usually defined as a quantity per unit length [DUF92]:

$$r_s = \frac{-E_{0z}^2}{dP/dz} = \frac{R_s}{d}, \tag{3.10}$$

where d is the length, r_s the shunt impedance per unit length, E_{0z} the amplitude of the axial electric field, and dP/dz the fraction of the input power lost per unit length in the walls. The minus sign means that the power, flowing along an RF wave structure, decreases due to losses.

Another important quantity is the quality factor Q. It is a figure of merit which relates the stored electromagnetic energy to the dissipated energy per unit length [DUF92]:

$$Q = -\frac{\omega w_s}{dP/dz}, \tag{3.11}$$

and

$$w_s = \frac{P}{v_g}, \tag{3.12}$$

where ω is the frequency of the RF wave, w_s is the stored energy per unit length. v_g is the group velocity of the wave, the velocity at which the energy is transported [DUF92].

The filling time t_f of a travelling wave structure is defined as

$$t_f = \frac{L}{v_g}. \tag{3.13}$$

The time t_f described the time duration which is necessary to fill up the whole structure with RF power.

3.3.2 Energy flow in a traveling wave LINAC.

Two types of travelling wave LINAC's are generally described: constant impedance and constant gradient structures. In this report only the constant impedance structure

will be treated. This type of structure offers because opportunity to handle each accelerating cell independly (i.e. a cell is regarded as a constant impedance structure), whereas for the constant gradient structure approximation the complete structure has to be treated as a whole.

As the wave propagates in a constant impedance structure, part of the input power is dissipated in the walls and the smaller power will lead to a smaller accelerating field in the next cells. Hence the accelerating gradient decreases along the structure. By combining equations (3.11) and (3.12) one can write:

$$\frac{dP}{dz} = -\frac{\omega}{v_g Q} P . \tag{3.14}$$

The solution of this equation is given by:

$$P = P_0 e^{-\frac{\omega}{v_g Q} z} , \tag{3.15}$$

where P_0 is the power fed into the LINAC. Combination of equation (3.10) and (3.14) gives the accelerating electric field:

$$E_{0z} = \sqrt{\frac{\omega}{v_g Q} r_s P} . \tag{3.16}$$

Now this solution is expanded, since in the first part of a travelling wave structure, for gradient β, the cells are not identical. But for each cell Q can be calculated with the computer code Superfish, as will be done in the next section. These values are also supplied by Philips Medical Systems-Radiotherapy (PSM-R) [BAT94], the manufacturer of the LINAC. Whereas v_g can be approximated with equation (3.17) or be measured.

To solve the problem of calculating of the amplitude of the electric field on the axis, it is assumed that equations (3.14) and (3.16) are still valid for a infinitesimal interval *dz*. The first order differential equation (3.14) can be solved by applying numerical programs such as Matlab. This is a mathematical tool to solve numerical mathematical problems.

So far energy transfer to the beam was excluded from our analyses, however it is an extra loss factor that has to be considered. When this energy absorption by the beam, which is called beam-loading, is taken into account the power diffusion equation becomes:

$$\frac{dP}{dz} = -\frac{E_{0z}^2}{r_s} - I E_{0z} \cos\varphi_s , \tag{3.17}$$

where I is beam current and ϕ_s is the average accelerating phase.

To solve this equation we make the assumption that for each interval *dz* the power dissipated in the wall is given by equation (3.14) and the axial electric fields can be calculated with equation (3.16). By inserting equation (3.16) into the power diffusion equation (3.17) the following equation is derived:

$$\frac{dP}{dz} = -\frac{\omega}{v_g Q} P - I \cos\varphi_s \sqrt{\frac{\omega}{v_g Q} r P} . \tag{3.18}$$

This equation is numerically solved by using the computer code Matlab. For each cell equation (3.18) is solved before the next cell. The output for one cell is input for the next and so on.

3.4 Results

By using the computer code Superfish it is possible to calculate Q for each accelerating cell. The codes solves the Maxwell's wave equation for a given frequency, in a structure with cylindrical symmetry and a conductor (copper) as boundary. It searches for a solution in the standing wavemode ($\pi/2$). From literature [DUF92] it is known that the quality factor Q remains the same for the $\pi/2$ (standing wave) and the $2\pi/3$ (travelling wave) mode. Since Q is only depended on the geometry of a cell for a given electromagnetic mode, in our case the TM_{01} mode.

The shunt impedance r_s is supplied by PSM-R (Table 3.1). It could not be calculated by Superfish, due to the fact that the shunt impedance r_s for the travelling wave mode is different from the one in standing wave mode and Superfish calculates the shunt impedance at the $\pi/2$ mode at resonance frequency. Whereas the travelling wave LINAC operates at a different frequency. For the last cells a comparison can be made with literature 71 MΩ/m [DUF92] and 60.2 MΩ/m [artikel]. The small difference between the Q values from PSM-R and Superfish are insignificant, since a error of 30 % is not unusual for calculations [LEE95].

Table 3.1: The shunt impedance and Quality factor calculated by Superfish and PSM-R for the first 14 cells (cell no 14 until 70 are identical).

Cellnr	r_s by PSM-R [MΩ/m]	Q by Superfish	Q by PSM-R
1	13.3	7468	7302
2	20.9	8820	8536
3	28.6	10073	9677
4	35.7	11140	10648
5	41.9	12016	11445
6	46.7	12670	12040
7	50.5	13331	12505
8	53.3	13670	12845
9	55.3	13962	13086
10	56.8	14019	13265
11	58.7	14205	13432
12	59.5	14196	13422
13	60.3	14187	13412
14	60.6	14183	13412

The group velocity of a disk-loaded cylindrical waveguide is calculated with the following approximation given by [DUF92]

$$v_g/c = \frac{(2a)^{3.23}}{891}, \tag{3.19}$$

where a is the iris diameter expressed in cm. This approximation is valid for a structure in the $2\pi/3$ mode at 3 Ghz. The result of this calculation is given in table 3.2.

Table 3.2: The approximated group velocity v_g.

Cell	v_g/c
1	0.014
2	0.014
3	0.014
4	0.014
5	0.014
6	0.014
7	0.014
8	0.014
9	0.013
10	0.012
11	0.011
12	0.011
•	•
70	0.011

To verify these values, the overall group velocity was measured. This was done by measuring the filling time of the accelerator: If the length L and the filling time t_f is known it is possible to calculate with equation (3.13) the average group velocity. The filling time was measured by determining the time difference between the ingoing and outgoing RF envelope for the accelerator waveguide. The result was 0.48 μs, which yields a group velocity v_g of $0.007c$. Which means that the accelerator tube is totally filled with RF power in 0.48 μs with a speed of $0.007c$. Compared with the calculated time difference of

$$t_f = \frac{L}{v_g} = \sum_{n=1}^{70} \frac{L_n}{v_{gn}} = 0.65\mu s, \tag{3.20}$$

This seems to agree reasonable. The difference is probably caused by not including the length and diameter of an accelerating cell in equation (3.19), because it is known from the dispersion relation (3.8) and equation (3.9) that this also of consequence for the group velocity.

After inserting these value into the power diffusion equation (3.18), the solution can be calculated with Matlab. In figure 3.5 the power and electric axial longitudinal field are shown with a beam current of 244 mA.

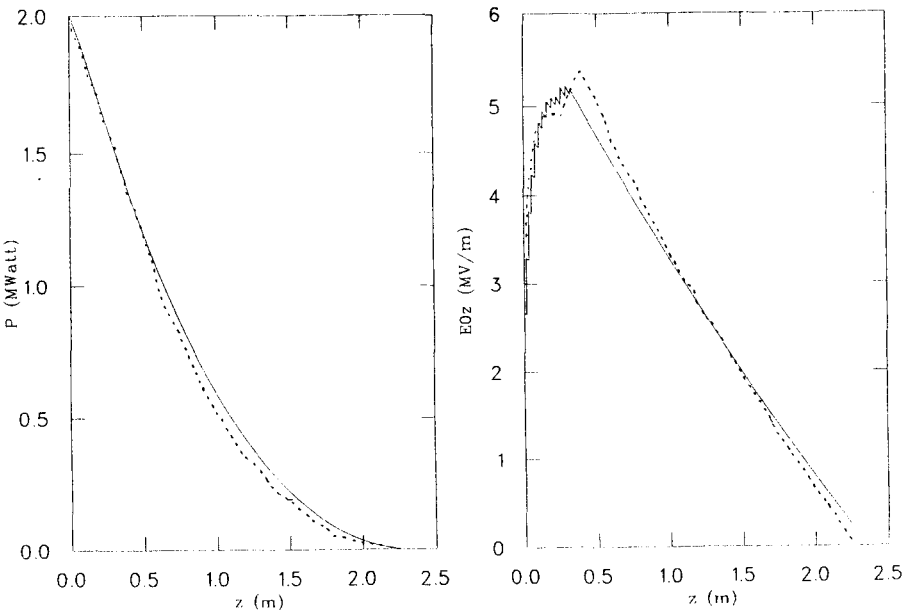

Figure 3.5 The power flow (left) and the electric axial longitudinal field by I beam=244 mA and $\phi_s=10^0$ [BAT94]. Continuous line is model TU Eindhoven, Dashed line is the model of PSM-R.

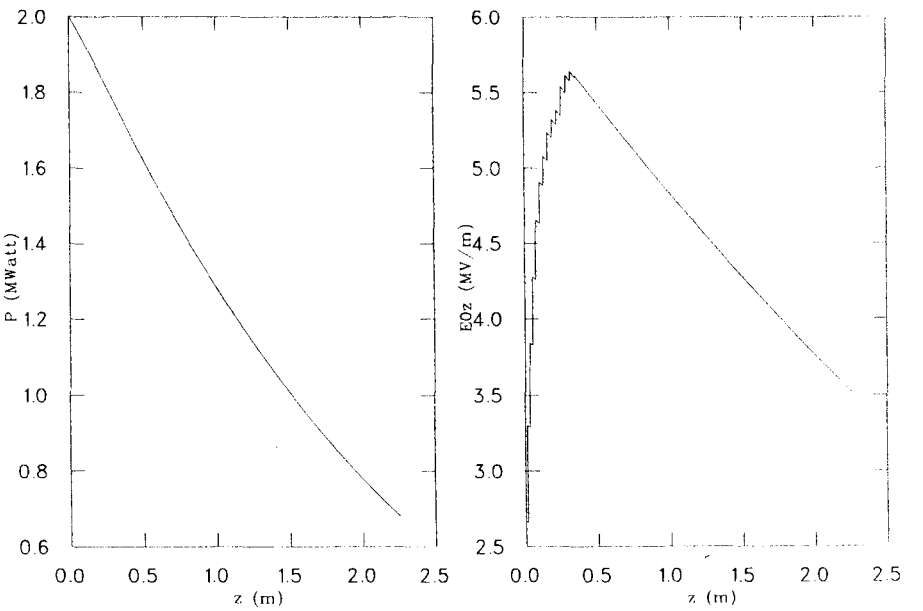

Figure 3.6 The power (left) and the electric axial longitudinal field for I =47 mA and ϕ_s $=10^0$

In figure 3.6 a beam current of 47 mA is used. At this current the LINAC delivers a beam with an energy of approximately of 10 MeV [Chapter 4]. From figures 3.5 it is clear that the data agree. These values can be inserted in the computer code Parmela. From the load-line, in section 5.3, which includes the results of this section, it can be concluded that there's an optimal point at about 6 MeV and 244 mA, at which the power transfer to the beam is 1.464 Mwatt and maximal.

4 Numerical calculations with the computercode PARMELA

In this chapter numerical simulations done with the computercode Parmela are presented. Parmela is used to calculate the phase acceptance of the LINAC, the energy spread, longitudinal and transverse emittance of the 10 MeV LINAC. Also the influence of the solenoids on the longitudinal acceptance has been investigated.

4.1 The computer code Parmela

The program Parmela, which stands for Phase and Radial Motion in Electron LINACs, is used to simulate the behaviour of the electrons in the 10 MeV linear travelling wave accelerator. Before Parmela can calculate the motion of the electrons, some input parameters are to be inserted. These input parameters contain initial phase and energy, position and impulse of all electrons.

Also each cell of the LINAC, with its Fouriercoefficients of the axial longitudinal electric field as calculated with Superfish (Chapter 3) has to be inserted in the input file with the input parameters. The magnitude of the electric field and the beam current is calculated with the theory described in chapter 3 in combination with Parmela: Parmela is used to calculate the stable phase φ_s of the electromagnetic wave, by doing this recursive the correct output energy of 10 MeV is reached.

With these Fouriercoefficients the electromagnetic field of each cell is calculated with the first and third Maxwell equations. The time dependence is given by a multiplication with the factor $e^{j\omega t}$. A time depended field map is made for each cell.

The magnetic field of the solenoids is inserted in the input file by using coils as mentioned in chapter 2. For each coil a map of the magnetic field is made by using equation (2.8) for a single coil. The longitudinal field of the coil is radially expanded by using the Taylor series of equations (2.10). Finally all magnetic fields are combined to one magnetic field map of the LINAC which is the sum of all single loop coil magnetic fields.

Parmela also has the option to include space charge calculations in the simulations. The space charge is calculated by making a electric field map generated by the electrons themselves. The motion of electrons in the LINAC is calculated by using the relativistic Lorentz force equation. The electric and magnetic fields are calculated by taking the total sum of all field maps which are mentioned. This is done for each time interval *dt*. Since time is the depended variable in Parmela.

4.2 Input distributions

In our simulations two kinds of starting distributions have been used. One is a rectangular array, generated by taking a Gaussian distribution with $r_{max}=0.1$ *cm* $<<\sigma_r$ $=5$ *cm* and $\varphi_{max}=360<<\sigma_\varphi=10000$.

Intermezzo: The Gaussian distribution is given by

$$f(z) = N_0 \frac{1}{\sqrt{2\pi\sigma^2}} \exp\left(-\frac{z^2}{2\sigma^2}\right), \qquad (4.1)$$

where z is the variable, $f(z)$ the probability times N_0 , which is the total number of particles, and σ, the standard deviation, is the parameter that defines the probability interval with boundaries $\pm\sigma$ in which 68% of the total number of particles is found. So if we don't take the whole z-axis but as boundary $\pm z_{max}$ we can change the distribution.

The energy spread and divergence is zero. This input distribution is used for the calculations of phase and energy spread and the longitudinal motion of the electrons. Since there is a tight beam and the electrons are injected continuously at the RF wave.

The other particle distribution is the Kapchinsky-Vladimersky (K-V) distribution [REI94]. This distribution has a uniform distribution in x-x',y-y' and x-y space. This distribution is commonly used in linear accelerators to make simulations of the transverse behaviour of the beam. To use this K-V distribution some parameters, like the emittance and the Courant-Snyder parameters, of the electron gun have to be calculated.

The electron gun used in the LINAC is a so-called Pierce-type. In a Pierce-type geometry, the electrodes form an angle of less than 90^0 with respect to the beam axis to produce a transverse electrostatic force that balances the repulsive Coulomb force due to the space charge of the beam, see figure 4.1 [REI94].

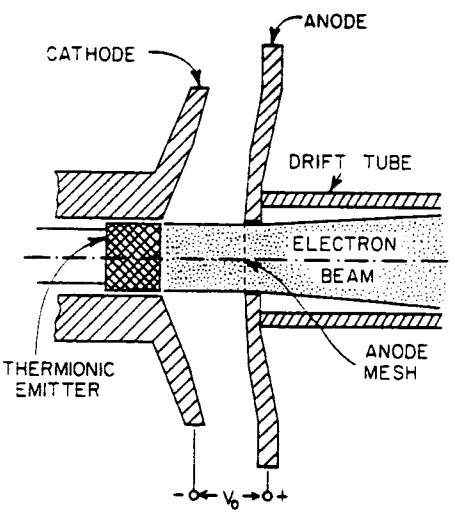

Figure 4.1 Schematic representation of an electron gun with thermoionic cathode, Pierce-type electrode geometry.

The electron beam radius in this example remains practically constant within the gun and then increases due to space-charge repulsion when the beam enters the field free region outside the anode. The beam has to be focused with, for example, solenoids.

Conduction electrons in a metal have an energy distribution that obeys the Fermi-Dirac statistics. The electrons emitted from a thermo-ionic belong to the Maxwellian tail of the Fermi-Dirac distribution, and the current density J_{th} is given by the Richardson-Dushman equation (4.2) [REI94].

$$J_{th} = AT^2 e^{-W/k_B T}. \tag{4.2}$$

Here T is the cathode temperature, W the work function of the cathode material (typically a few eV) and k_B is Boltzmann's constant ($8.6175.10^{-5}$ eV/K). The theoretical value for A is $1.2.10^6$ $Am^{-2}K^{-2}$.

An important figure of merit for a beam is the emittance, which is basically defined by the product of the width and transverse velocity spread of the beam. The electrons in the tail of the Fermi-Dirac distribution inside a cathode have a Maxwellian velocity distribution given by

$$f(v_x, v_y, v_z) = f_0 \exp\left[-\frac{m(v_x^2 + v_y^2 + v_z^2)}{2k_B T}\right]. \tag{4.3}$$

As a result the particles emerge from the source with an intrinsic energy spread. If x and y denote the two Cartesian coordinates perpendicular to the direction of the beam, the rms. values of the transverse velocity spread for the Maxwellian distribution are found to be [REI94]

$$\bar{v}_x = \bar{v}_y = \left(\frac{k_B T}{m}\right)^{1/2}. \tag{4.4}$$

If the emitting surface is a circle with radius r_s, and with uniform current density as we presume for the LINAC, the rms. width of the beam is

$$\bar{x} = \bar{y} = \frac{r_s}{2}. \tag{4.5}$$

The effective normalized rms. emittance is defined relativistically as

$$\varepsilon_{rms,n} = \frac{r_s}{2}\left(\frac{k_B T}{mc^2}\right)^{1/2}. \tag{4.6}$$

The normalized emittance measures the beam quality in two-dimensional phase space, which is defined by the space and momentum coordinates of the particle distribution (i.e., x,p_x, or x,v_x, nonrelativistically). From Liouville's theorem it may be shown that the normalized emittance remains constant if there are no nonlinear forces between different coordinate directions [REI94].

In the case of our LINAC, the normalized rms. emittance of the gun can be calculated with equation (4.6). The temperature T of the anode is about 2000 K, mc^2 =

$T+E_0=45+511$ = 556 keV and $r_s=3.75.10^{-3}$ m. This gives a normalized rms. emittance $\varepsilon_{rms,n}$ of 1 mm.mrad. The normalized emittance ε_n is 4 mm.mrad.

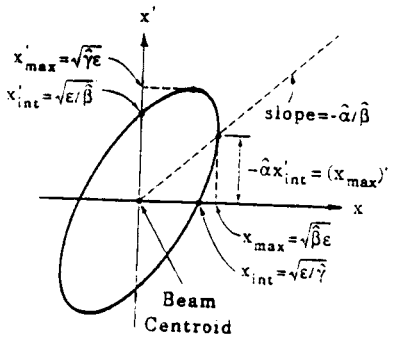

Figure 4.2 Trace space ellipse and relations for several important points on the circumference of the ellipse.

The next step is the calculation of the Courant-Snyder parameters γ, α and β . These parameters determine the shape of the trace space ellipse, see figure 4.2, which surface is the emittance. The equation of this ellipse is

$$\hat{\gamma}x_{rms}^2 + 2\hat{\alpha}x_{rms}x'_{rms} + \hat{\beta}x'^2 = \varepsilon_{x,rms,n}, \qquad (4.7)$$

, where α is taken to be zero at the gun.

Two unknown parameters remain in equation (4.7). But x_{rms} is known, because a K-V distribution is assumed, what means that in the x-y plane we also have a uniform distribution. So $x_{rms}=\frac{1}{2}\sqrt{2}\,r_s=2.65.10^{-3}$ m. This gives a γ of 0.14 mrad/mm., with this β can be calculated to be $1/\gamma$=7.02 mm/mrad. These parameters can be inserted in Parmela.

4.3 Phase acceptance and energyspread of the LINAC

To determine the phase energy relation, a bunch of electrons is injected at a certain phase φ of the RF wave. The bunch is created by taking a Gaussian distribution as mentioned in the former section, but with the difference that φ_{max} is 1^0 instead of 360^0.

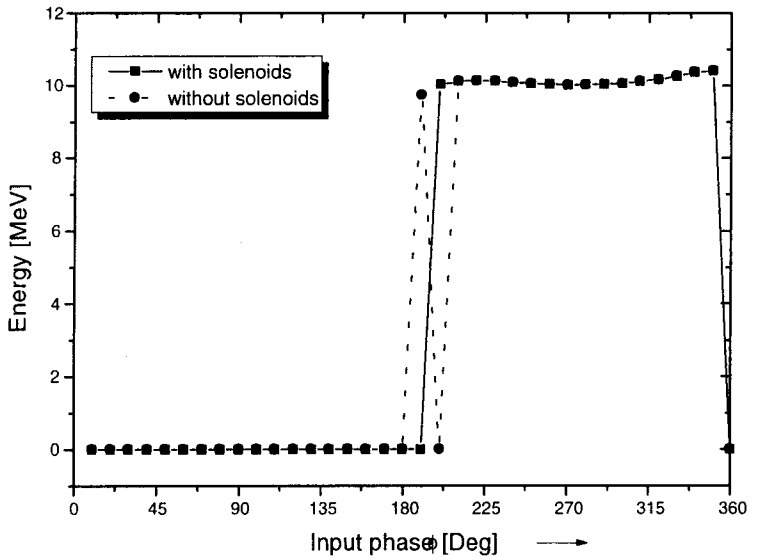

Figure 4.3 The input phase-energy relation.

From figure 4.3 it can be seen that there's almost no difference in longitudinal acceptance between the simulations with or without solenoids. Only in the transition area between 180 and 200 degrees a difference is present. From figure 4.5 it can be concluded that the small peak at 180 degrees has only a very low intensity.

The fact that the interval at which electrons are accepted by the LINAC is 160^0 is very interesting if one considers that the stable bucket area is about 20^0 . This means that electrons move over the electromagnetic wave and can be caught into the bucket.

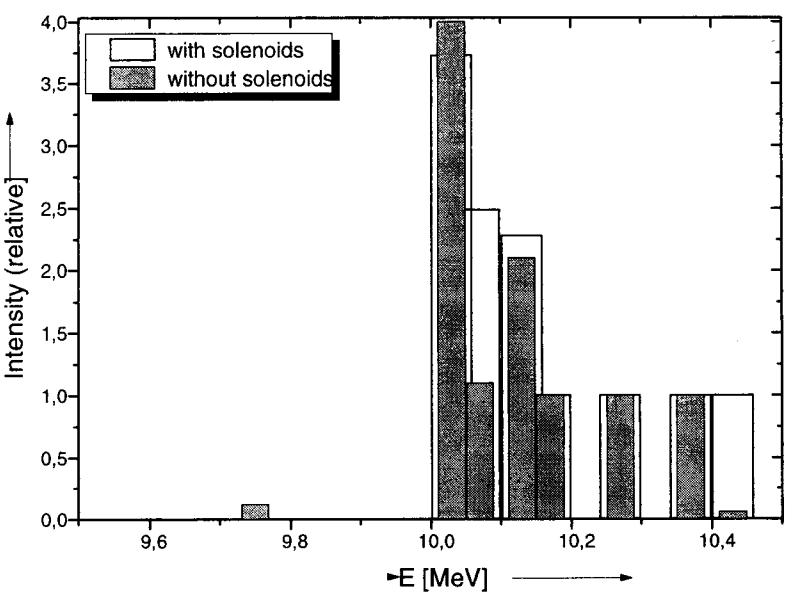

Figure 4.4 Normalized intensity versus energy.

From figure 4.4 it seems that the influence of the solenoids is a greater output current and a somewhat larger energy energyspread. The very small number of electrons with a low energy does not change this conclusion. In the general shape of the energy intensity distribution no great differences are to be found. One can conclude that the solenoids have no great influence on the longitudinal behaviour of the LINAC.

From the same calculation also the input phase-normalized intensity relation can be found, as depicted in figure 4.5. From this figure it can be concluded that solenoids cause a smoother input phase-normalized intensity curve. This is probably caused by the focusing action of the solenoids, which centers the electrons at the axis of the beam, so less electrons experience off-axis fields, which can distort the acceleration process positively or negatively.

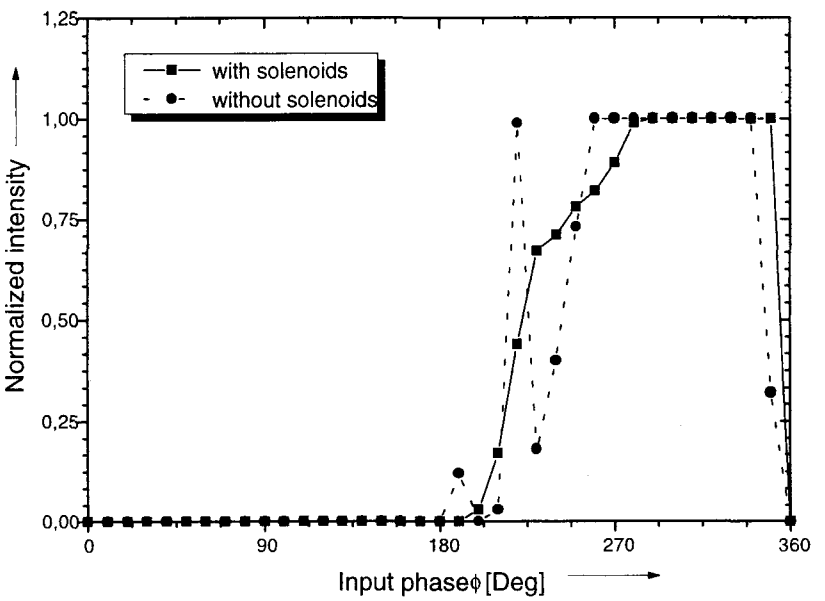

Figure 4.5 The input phase-normalized intensity relation.

4.4 Longitudinal emittance.

For the calculation of the longitudinal emittance , the K-V distribution, as described in section 4.2, is used as input beam. The result of the calculation is shown in figure 4.6.

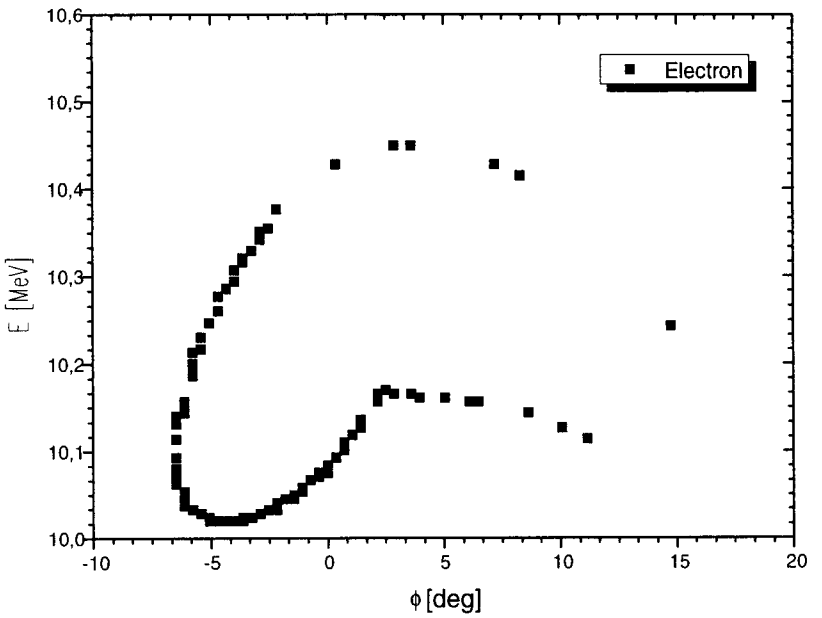

Figure 4.5 The calculated longitudinal emittance of the LINAC with φ the phase on the RF wave.

From figure 4.5 we may conclude that the longitudinal emittance is partly within the desired values as given by the calculated acceptance of RTME, which means an energy of about 9.96 MeV±1% and a total phase spread of 18^0 [WEB94]. From figure 4.5. it is seen that a large part of the electrons are within this RTME acceptance. Furthermore a tail is seen. This tail consists of electrons who leave the bunch and will fall back into the next bunch.

4.5 Transverse Emittance

For the calculation of the transverse emittance in the x- and y-direction, again the K-V distribution as mentioned in the former sections is used. The emittance is calculated at 10 points along the LINAC to gain insight in the changes in phase space during the accelerating process. The emittance in x- and y-direction is shown in figure 4.6 and 4.7

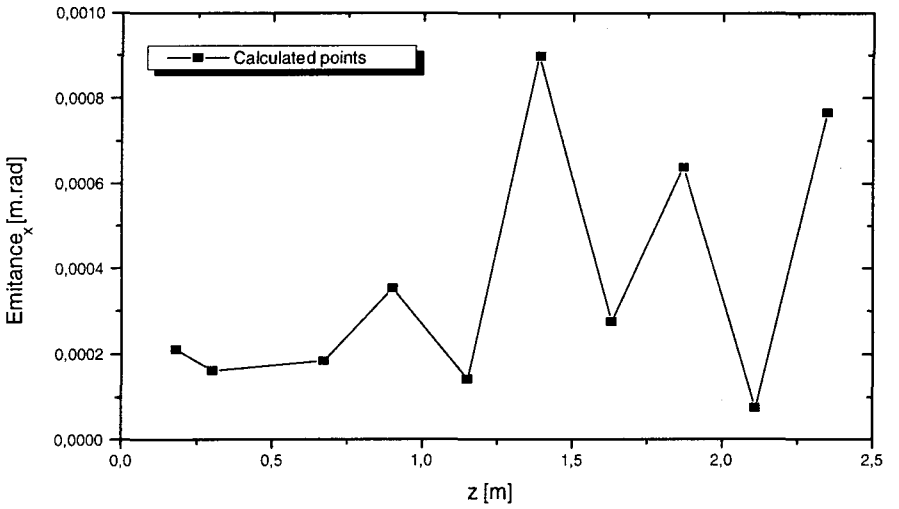

Figure 4.6 The emittance in x-direction along the LINAC.

As we can conclude, the transverse emittances varies a lot along the LINAC. The three two-dimensional phase spaces (x,x'),(y,y'),(φ,ΔE) are coupled in the LINAC. And during the accelerating process a continuous interchange between the different phase spaces take place. It is difficult to draw any conclusions from these figures.

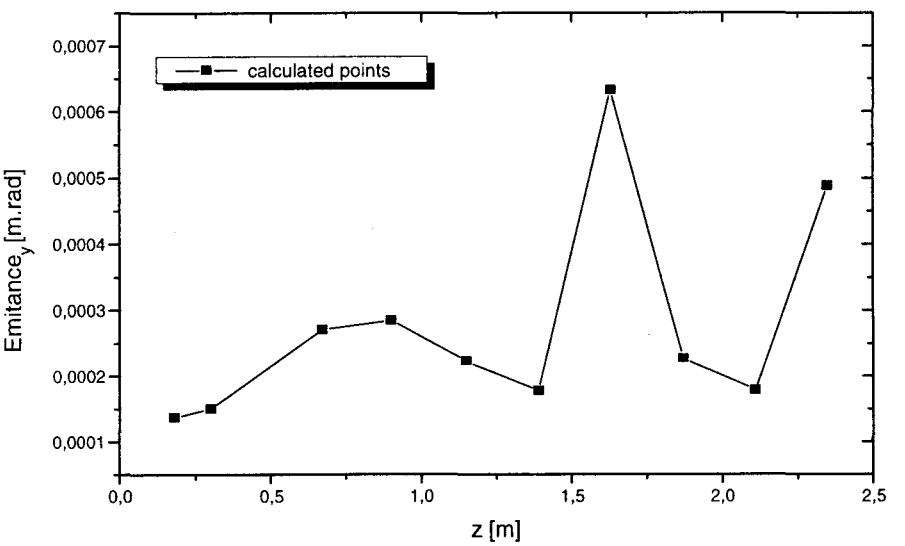

Figure 4.7 The emittance in y-direction along the LINAC.

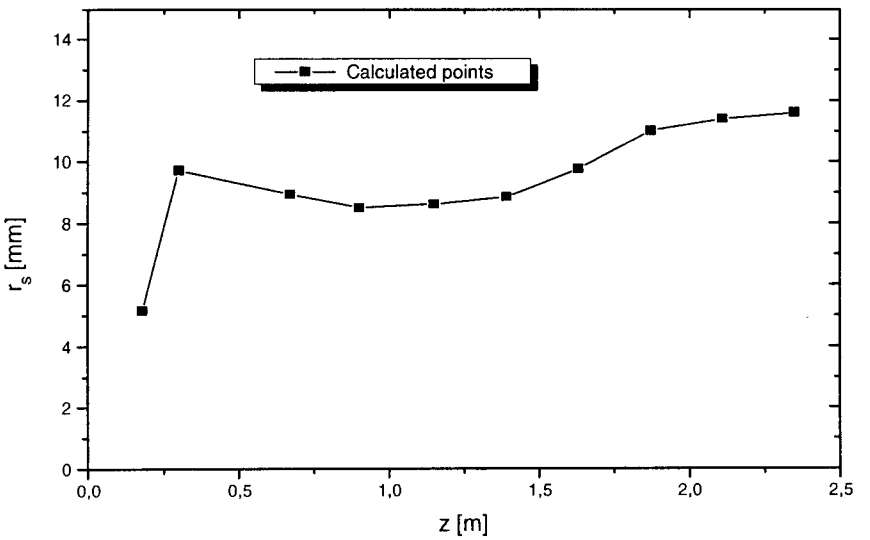

Figure 4.8 The beam radius r_s as function of distance along the LINAC.

The beam radius as function of the distance along the accelerator, exhibits a smoother pattern. After an initial blow up, due to a defocusing related with the longitudinal bunching, a great number of particles are lost. Then the beam shrinks under the influence of the solenoids. As shown in figure 2.5 the solenoids get weaker to the end and the beam now starts to grow steadily.

5 Electron Beam Measurements on the 10 MeV LINAC

In this chapter measurements on the electron beam of the LINAC are presented. First the beam current as a function of the heating current of the electron gun is measured with a Faraday cup. Also the relation between the beam current and the remaining RF power behind the LINAC is measured with this setup. The optimized operating frequency of the LINAC is determined. With a different setup, consisting of a bending magnet and a slit, the energy spectrum of the electron beam is determined for different heating currents, in order to reconstruct the load-line. Finally the beam diameter is measured with a movable tantalum plate.

5.1 Beam current versus gun heating current.

In our experiments a Faraday cup was used to determine the shape and height of the current pulse generated by the LINAC. A Faraday cup is in essention a piece of material that fully stops the electron beam. The magnetron and therefore also the electron beam is pulsed. The length of this pulse is approximately 2 μs, and therefore contains a great number of RF periods [COP92]. Within these periods the electrons are bunched into groups with limited phase extend, i.e. micro structure.

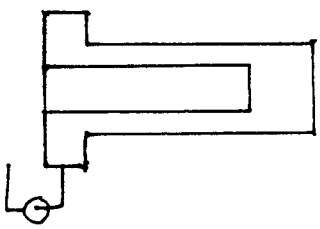

Figure 5.1 The Faraday cup.

We are interested in the envelope of the macropulse, not in the more detailed fine, or micro structure. See figure 5.1 for a schematic representation of the faraday cup and figure 5.2 for an oscilloscope graph of the macropulse.

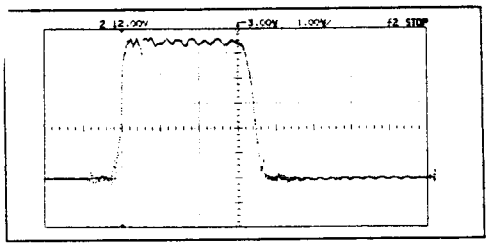

Figure 5.2 The macro structure of the pulse.

A measurement was done to determine the beam current dependence of the heating current of the gun.. The heating current was measured with an ampere meter before and after the HT pulse was applied, this to check if the current remains constant. While applying the HT pulse the ampere meter was disconnected to avoid damage. The beam current was determined from the amplitude of the voltage pulse on the Faraday cup.

The transmission system of the Faraday cup, which is interpreted as a current source. is depicted in figure 5.3. We need a balanced transmission system in order to be able to distinguish the pulse from the background noise. This system consists actually of two parallel twisted 51 Ω transmission lines. One is connected to the Faraday cup. The other is connected to a capacity of 4.7 pF which simulates the capacity of the Faraday cup. Both elements are followed by the transmission line with at begin and end a 51 Ω resistor, which equals the characteristic impedance of the line. The two lines are interconnected by a 150 Ohm resistor, which balances the lines with respect to each other.

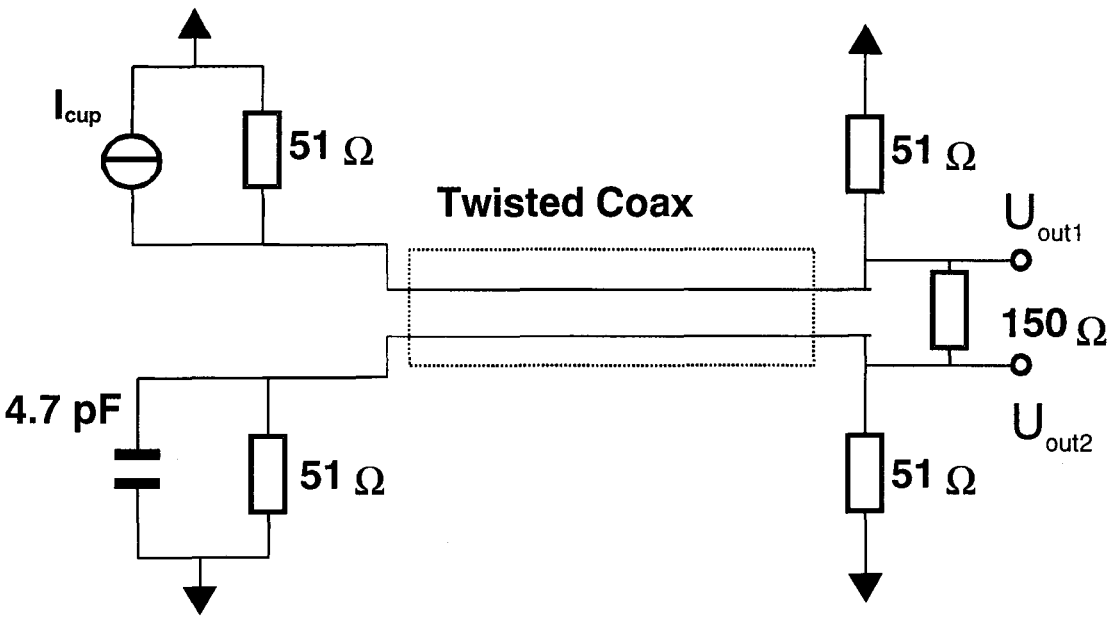

Figure 5.3 The transmission line from the Farady cup to the measure equipment.

By using a differential amplifier the signal from the condsensator is inverted and subtracted from the signal from the Faraday cup. The output impedance of the total transmission system equals 19.0 Ω [Appendix A]. For a remaining noise level of 0.9 mV, this means we are able to detect a current of 50 nA in the macropulse.

The results of the dependence of the beam current on the heating current of the electron gun are depicted in figure 5.4. The function is not linear but the cup current seems to be exponential, see section 4.3.

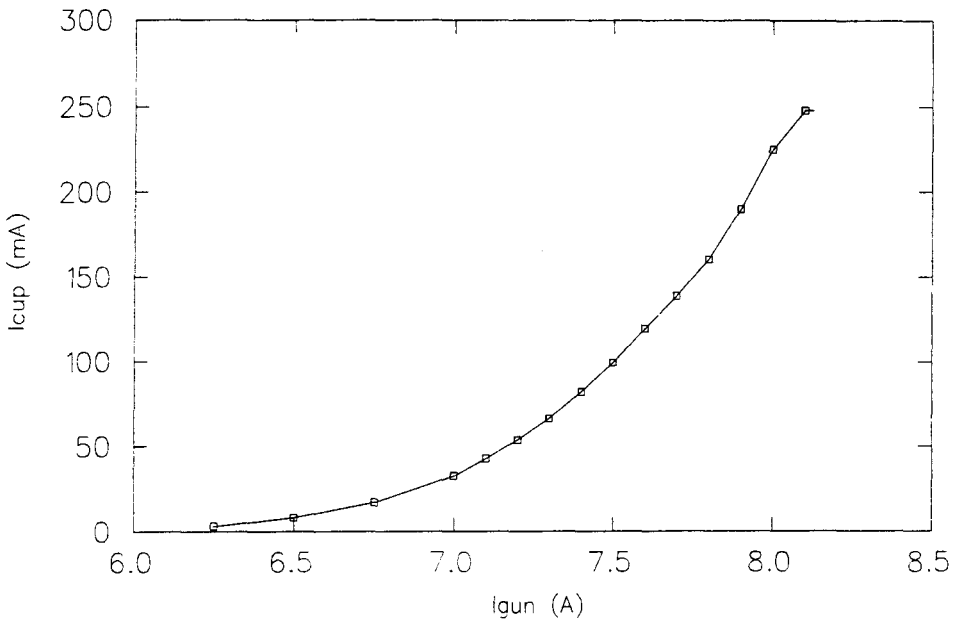

Figure 5.4. The beam current I_{cup} as a function of the heating current I_{gun} of the electron gun.

5.2 RF measurements

In this section two series of measurements are presented. One in which the outcoming RF power is measured as function of outcoming beam current. The other concerns the magnetron frequency dependence of the LINAC. The outcoming beam current was measured as function of the magnetron frequency.

The beam current was measured with the Faraday cup. The outcoming RF power was measured with a RF detector before the RF dump at the end of the LINAC, see figure 1.3. The beam current was varied by changing the heating current of the electron gun. The result of the measurement is given in figure 5.4.

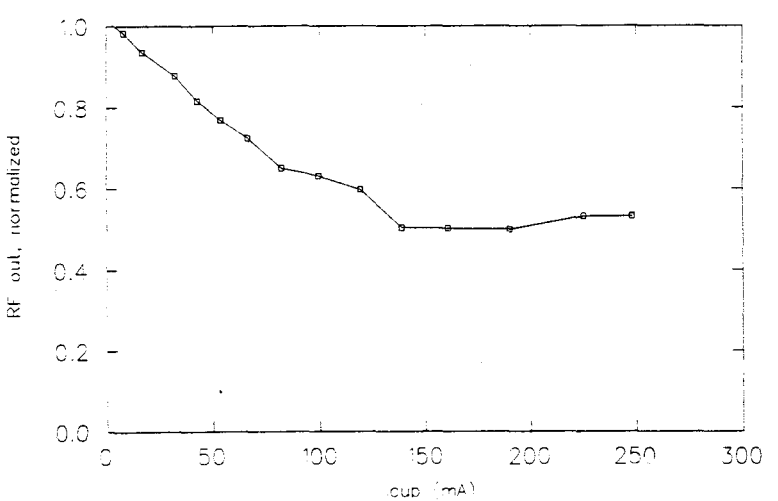

Figure 5.5. The outcoming RF power as a function of the current at the Faraday cup.

From figure 5.5 it can be concluded that when the beam current is zero the outcoming RF power is maximal and when the beam current is maximal the outcoming RF power is minimal. This is as expected from the calculations in section 3.3. Note however, that for more quantitative results the circuit of the RF pick-up, cable and detector would have to be calibrated. The relationship is not linear. That means that the power transfer from the RF wave to the electron beam is linear.

Also the frequency dependence of the LINAC was measured. this to find the operation frequency of the LINAC, and therefore also of the accelerating structure of RTME. The frequency of the magnetron can be varied by moving a capacitive plunger in and out. This plunger is stepper motor controlled.

The beam was measured at the Faraday cup and the frequency was measured by using a calibrated high quality resonant absorption cavity connected to the pick-up electrode behind the magnetron (see figure 1.3). The measurement is depicted in figure 5.6. A plateau is seen in where the beam current does not change. The operation frequency is defined as the middle of the plateau and is 2998.3±0.2 MHz.

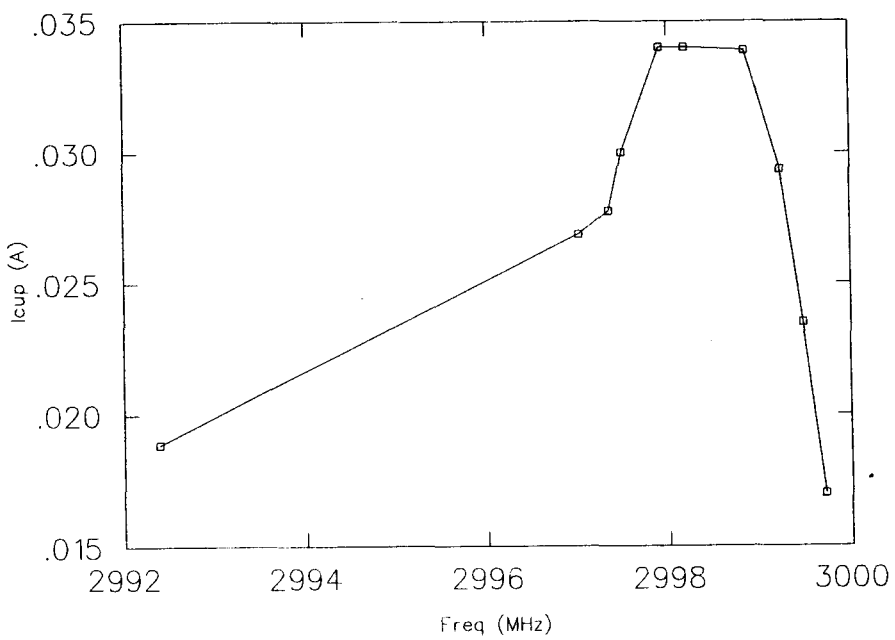

Figure 5.6 The magnetron frequency dependence of the LINAC with the measured beam current as reference for good operation.

5.3 Energy spread

In order to determine the load-line of the 10 MeV LINAC, i.e. the output energy as a function of the beam current, the peak energy is measured as a function of the beam current. The peak energy is determined with the setup depicted in figure 5.7. Due to the dispersive action of the dipole magnet the foci of the different energies will be spatially separated for a parallel input beam.

By selecting part of the focus range with a 1 mm slit, part of the energy spectrum is selected. The related current is measured on the Faraday cup, behind the slit. By scanning the beam with the dipole magnet across the fixed slit the complete energy spectrum of the beam can be determined.

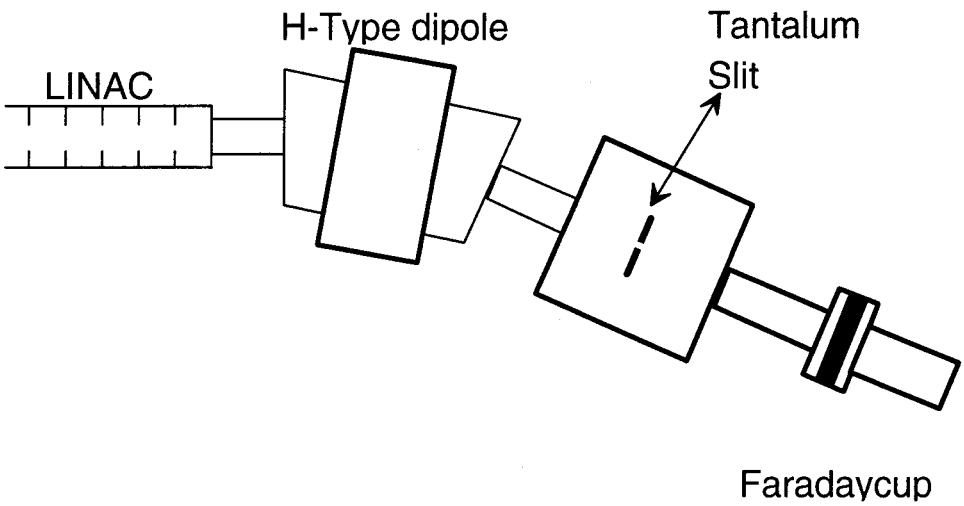

Figure 5.7 Experimental setup energy spread measurement.

In order to be able to apply equation 2.3 to determine the momentum (energy) of the electron beam, the true field profile of the dipole has to be replaced by a rectangular field profile with equal surface [THE94].

Another option is to relate the current through the windings of the dipole and the measured field map of the dipole via numerical calculations to the central bending energy of the beam to the current through the coils of the dipole magnet, see figure 5.8.

A disturbing effect has to be regarded. Due to the fact that the beam is not parallel but has a certain divergence the measurement will be distorted. Now electrons with different energy and nonzero divergence can reach the Faraday cup. Which means that the measured energy spectrum is distorted by electrons with a nonzero divergence.

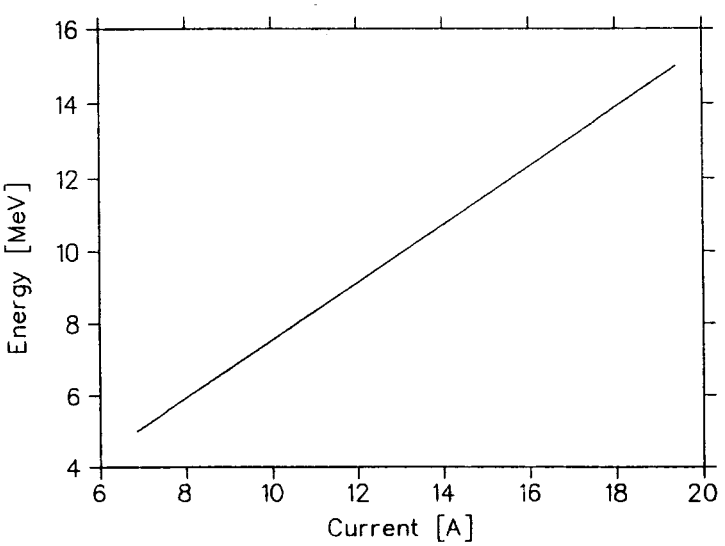

Figure 5.8 The electron energy (MeV) versus dipole current (A) curve.

The beam current after the bending dipole is measured at two locations. The first location is the tantalum slit. All electrons that are stopped induce a current which is measured with an oscilloscope. The electrons that are going through the slit are detected and measured by the Faraday cup, as described in section 5.1.

The energy spectrum of the electron beam was determined for several heating currents, fig 5.9 and 5.10 show some results.

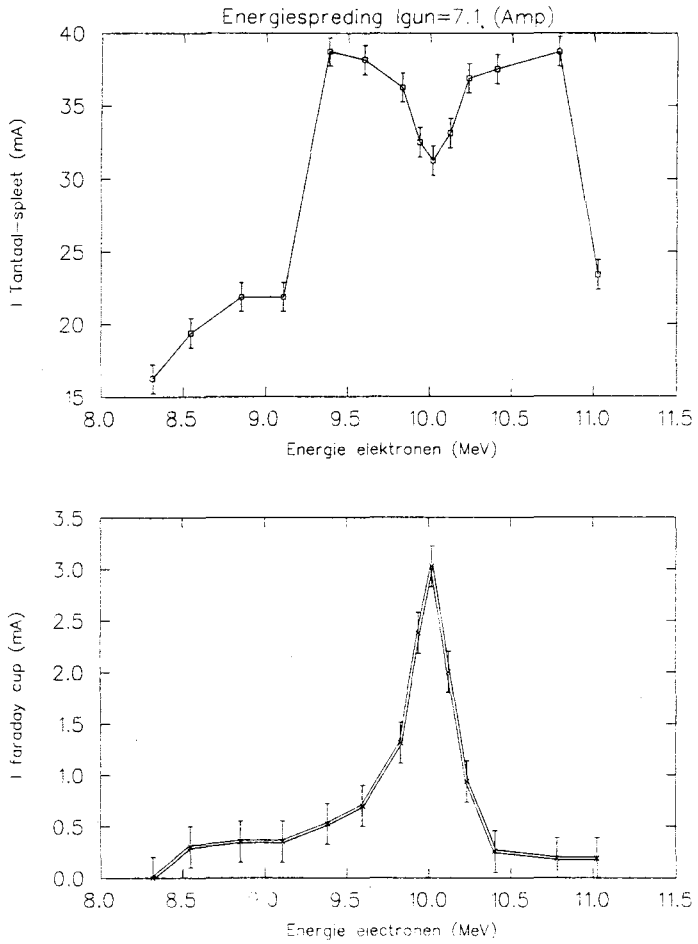

Figure 5.9 Beam current on the tantalum metal around the slit upper) and beam current on the Faraday cup for a heating current of 7.1 A.

From figure 5.9 it can be concluded that the energy peak is 10.1 MeV. The FWHM energy spread is 3.5 %. We see a low energy tail and a high energy part. The total energy spread is about 2.5 MeV. If we look at the current at the tantalum slit, we see that there's a local minimum, when there's a maximum at the Faraday cup. However the total of both currents is not constant. This is probably caused by losses after the slit.

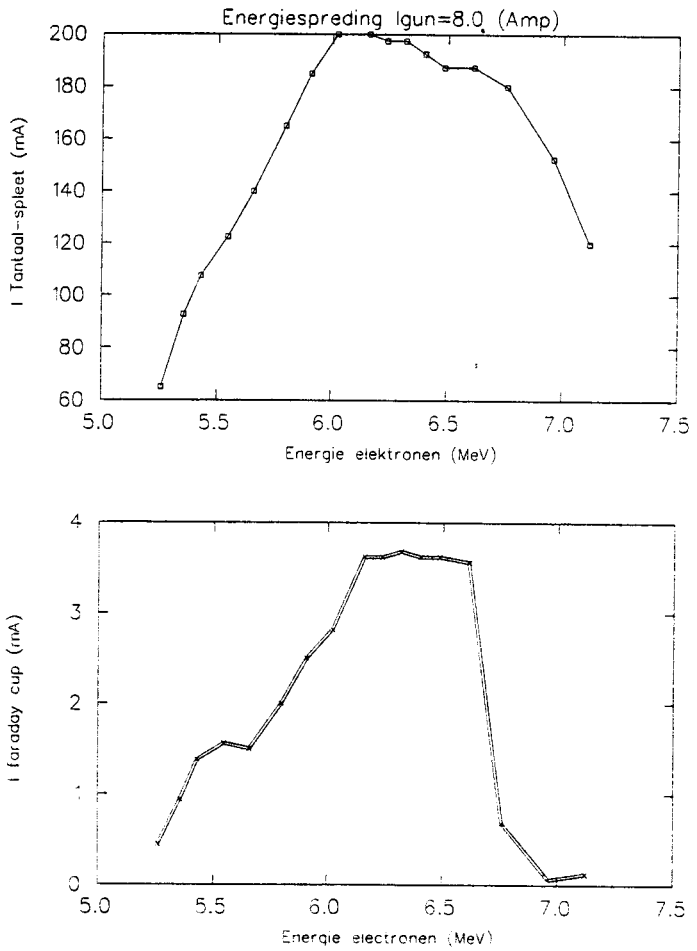

Figure 5.10 Beam current on the tantalum metal around the slit upper) and beam current on the Faraday cup for a heating current of 8.0 A.

Picture 5.10 shows us that there's no real maximum in the current of the Faraday cup, but a plateau, where the beam current is constant. The length of the plateau is 0.5 MeV. The total energyspread is 2.7 MeV. The current on the tantalum slit has no local minimum as in figure 5.9. One of the causes is the great energy spread at this heating current of 8.0 A.

By measuring the energy spectrum of the beam for several heating currents (which means different beam currents). the peak energy can be plotted as a function of the beam current, this is the so-called load-line. Fig 5.11 depicts the measured and calculated load-line of the LINAC. As can be seen the agreement is very good.

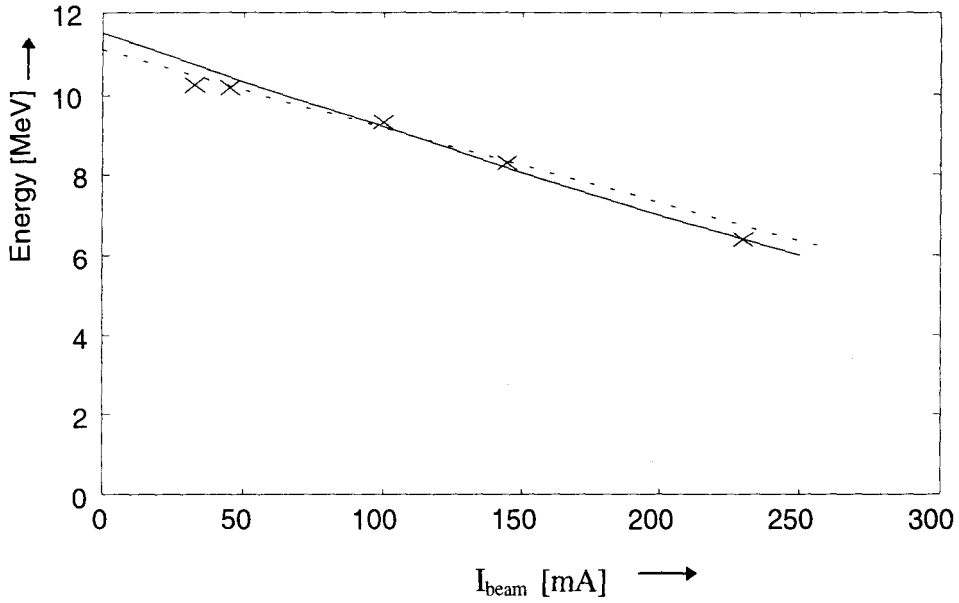

Figure 5.11 The load-line of the 10 MeV LINAC. The solid line is the data from PSM-R [BAT95], the dotted line is calculated with the model from chapter 3 and the crosses are measured.

5.4 Beam diameter.

The beam diameter is measured with the experimental setup as depicted in figure 5.12. Beam currents are measured likewise as in section 5.3. The currents on both the tantalum plate and the Faraday cup are measured on an oscilloscope on which the voltage amplitudes of the signals can be seen. This value can be transformed to a current with the output impedance of the total transmission system as described in section 5.1. The position of the tantalum plate is determined by processing the output voltage of the potentiometer with a reference voltage. The potentiometer is connected to a stepper motor which drives the insertion arm. The reading of the potentio meter to control the stepper motor is done by a hardware unit.

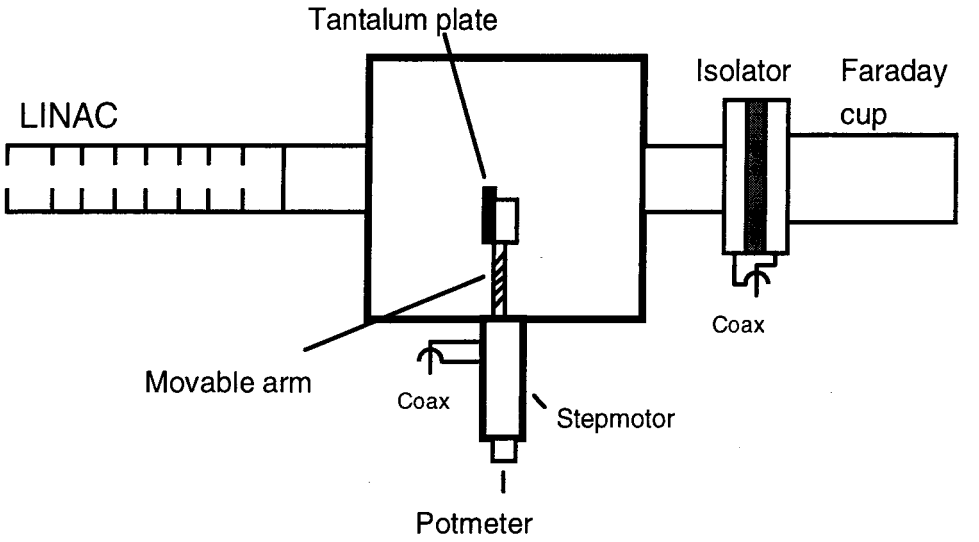

Figure 5.12 The experimental setup for the beam diameter measurement.

This diameter measurement was done for several gun heating currents. This to investigate what the effect of different beam currents and therefore energies on the diameter of the beam. A difference is expected due to the greater focusing power of the solenoids if the beam current is increased, since a higher beam current leads to a lower energy of the electrons (See chapter 3).

The results of the measurements with a gun current of 7.0 (A) and 8.0 (A) are depicted in figure 5.13 and 5.14. The current values are normalized to the total current on both tantalum plate and Faraday cup.

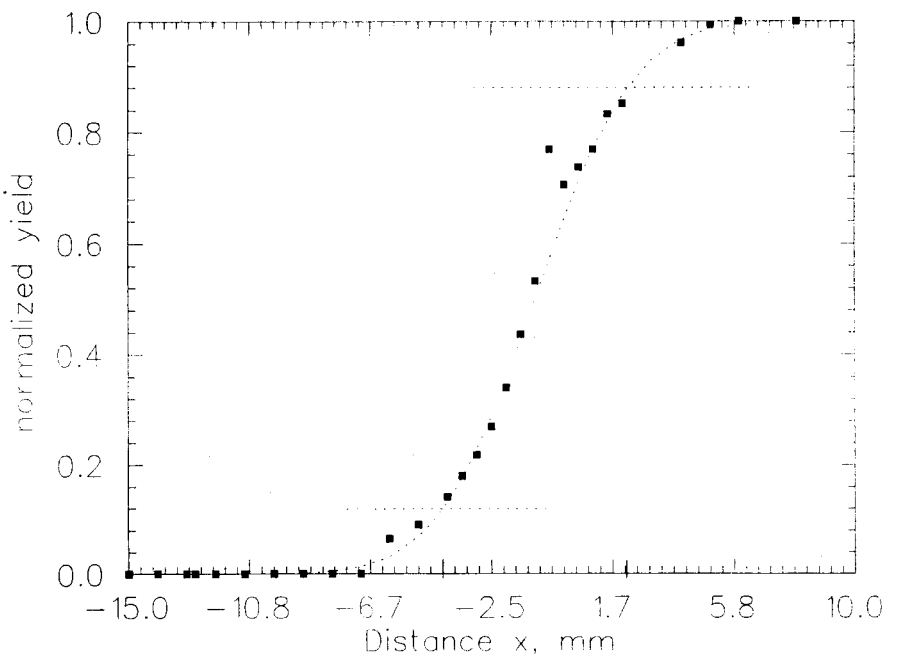

Figure 5.13 Normalized beam current as function of insertion distance of the tantalum plate for a heating current of 7.0 Amperes.

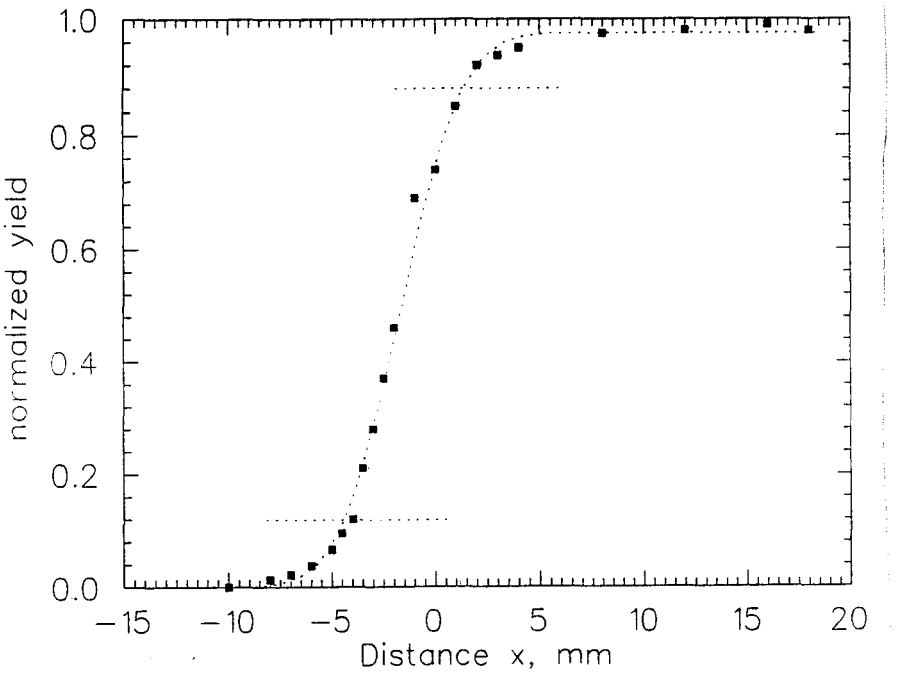

Figure 5.14 Normalized beam current as function of insertion distance of the tantalum plate a heating current of 8.0 Amperes.

Also a point of interest is the influence of reducing the current through one group of solenoids. The default values of the current through the solenoids is 20.0 A for the first one, 14.5 A for the second three and 17.5 A for the last four solenoids. If one of them is changed a different diameter is expected, since the focusing power of one group of solenoids is reduced. So an increase of beam diameter is expected. In one experiment the current through the last four solenoids was changed from 17.5 to 6 Amperes. The result is depicted in figure 5.15

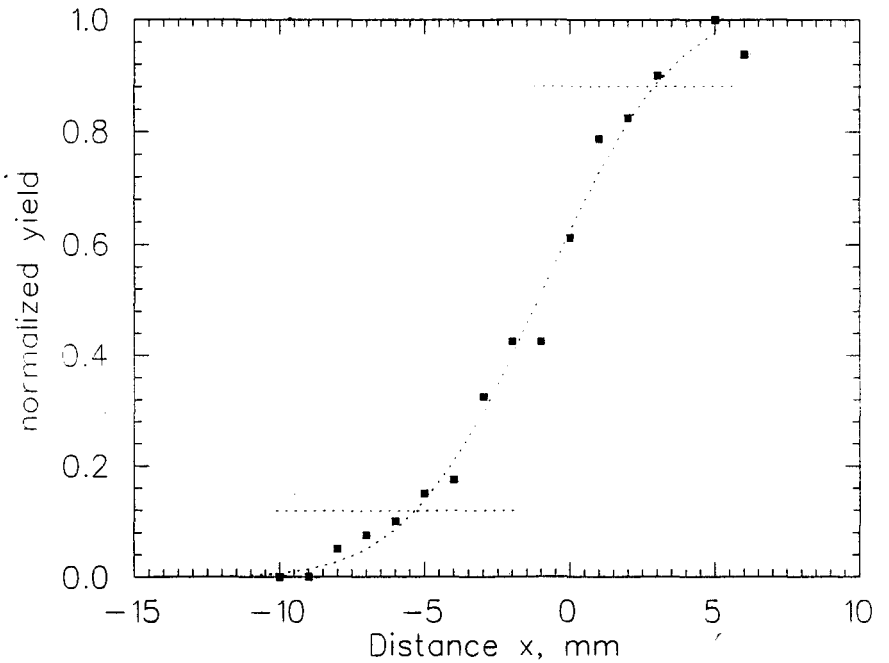

Figure 5.15 Normalized beam current as function of the insertion distance of the tantalum plate at a gun heating current of 7.0 A and a current of 6 Amperes through the last four solenoids instead of the default value of 17.5 A.

The function with which the graphs are fitted is a error function. To deduce the diameters two dotted lines are depicted at the FWHM. By determining the difference between the two lines, the diameter is known. The results are given in table 5.1.

Table 5.1 The beam diameter as function of heating current and current of the last four solenoids.

	I_{gun} (A)	I_{focus3} (A)	FWHF diameter (mm)
1	7.0	17.5	6.2
2	8.0	17.5	5.4
3	7.0	6.0	8.4

These results show that the influence of the solenoids is greater at lower electron energy (higher heating current). This is also what was expected. Also the greater the current through the solenoids the smaller the beam diameter is if one keeps the gun heating current constant.

6 Conclusions

For a proper injection of the output beam of the LINAC into the racetrack microtron Eindhoven (RTME) the characteristics of the output beam has to be known and the working of the accelerator has to be understood. Therefore in this report a lot of measurements on individual components of the LINAC, electron beam measurements and beam dynamic simulations with a computer code are presented.

From the magnetic field measurements of the steering magnets it appears that their steering capacity is sufficient. However, due to the correction for the earth magnetic field, it is not necessary to use the first pair of steering dipoles. The second pair of bending magnets will be used to steer the beam correctly into the beam guiding system toward the microtron.

The magnetic fields of the solenoids have been measured and parametrised as single loop coils, to be used as input for the simulation computer code Parmela.

The shape of the electric fields has been determined with the program Superfish, based on the asssumption that the geometry of the LINAC is periodic. This is true for most of the waveguide. However, not for the buncher section, the influence of this approximation should be investigated.

The calculation of the electric field strength and power flow by the numerical solution of the power diffusion equation agrees bvery well with the data provided by the manufacturer, which where obtained on basis of a coupled pillbox model.

Also the mesaured, calculated and supplied load line agree very well. For examplee, the measured current at 10 MeV is 45 mA, where the model predicted a current of 47 mA.

The simulations in longitudinal phase space point out that the electrons over almost 180 degrees of the RF period are captured. The longitudinal emittance calculated is larger than the acceptance of RTME, the measurements suggest an even worse longitudinal behaviour of the LINAC. Therefore it is wise to cut in the longitudinal phase space before the beam enters the microtron, to avoid excessive radiation production

Statements about the behaviour in transverse phase are hard to make. The simulated beam radius tends to agree well with the measured beam radius. It is not possible to draw any conclusions from the calculated transverse emittance figures, there are to many unknown parameters.

A more detailed study on the particle dynamics should be caried out in order to understand the behaviour of the machine completely.

References

[BAT93] Personel communications with Dr.T. Bates.

[BOT88] Botman J.I.M., Hagedoorn H.L., *Lecture notes on ion optics*, Eindhoven University of Technology (1988)

[BOT89] Botman J.I.M., Hagedoorn H.L., *General purpose storage ring as post accelerator for the ILEC cyclotron*, Proc. of the 1989 Int. Conf. on Cyclotrons and their Applications, Berlin (1989) 43-46.

[COP92] Coppens, J. *Measurements of the macropulse current and structure of a medical LINAC*, Internal report VDF/NK 92-27, Eindhoven University of Technology 1992

[COP94] Coppens, J.E. *Design study for the accelerating cavity of the racetrack microtron Eindhoven*, VDF/NK 94-18 MSC. Thesis, Eindhoven University of Technology (1994).

[GRA95] Graus J.M.H., *Bedieningsinstructies LINAC 10*, Internal report VDF/NK 94-47 (in dutch), Eindhoven University of Technology (1995).

[HEY89] Van der Heide J.A., Kleeven W.J.G.M., de Regt R.J.L.J., Magendans P., *The Eindhoven minicyclotron ILEC*, Proc. of the 1989 Int. Conf. on Cyclotrons and their Applications, Berlin (1989) 121-124.

[JAC89] Jackson J.D., *Classical Electrodynamics*, John Wiley & sons Inc., page 503-560 (1975)

[KEM95] Personel communications with Ing. A. Kemper.

[LAP70] Lapostolle P.M., Septier A.L. editors ,*Linear Accelerators*, North-Holland Publishing Compagny (1970) Amsterdam.

[LEE95] Personel communications with Ir. R.W. de Leeuw.

[LEE96] Leeuw de R.W., Ph.D. Thesis, Eindhoven University of Technology (1996).

[MUT95] Mutsaers, P.H.A., *Design and realisation of the Eindhoven scanning proton microprobe*, Ph.D. Thesis, Eindhoven University of Technology (1995).

[NEV95] Nezhevenko O., et al., *TW Accelerating Structures with minimal surface electric field*, PAC conf. 1995

[PAR94] Manual Parmela (1994)

[PER68] Persico E., Ferrari E., Segre S.E.,., *Principles of particle accelerators* , W.A Benjamin 1968

[POZ93] Pozar, D.M., *Microwave Engineering*, Addison-Wesley Publicing Compagny (1993) New York.

[REI94] Reiser, Martin, *Theory and design of charged particle beams*, John wiley & Sons Inc (1994) New York

[THE94] Theuws, W.H.C. *Beam positioning and beam monitoring in the racetrack microtron Eindhoven*, Internal Report VDF/NK 94-36, M.Sc. Thesis, Eindhoven University of Technology (1994).

[WAL48] Walkinshaw W., *Theoretical Design of LINAC Accelerator,* Proc. Phys. Soc. (London) 61.246 (1948)

[WEB94] Webers, G.A., *Design of an electron optical-system for a 75 MeV racetrack microtron*, Ph.D. Thesis, Eindhoven University of Technology (1994).

[WIN78] Grote Winkler Prins Encyclopedie, Elsevier, 8^{e} druk 1978

Appendix A: The Measurement Transmission line

In this appendix it is shown that the resistance of the transmision system is 19.03 Ω. We start from the transmission network, as shown in figure A1

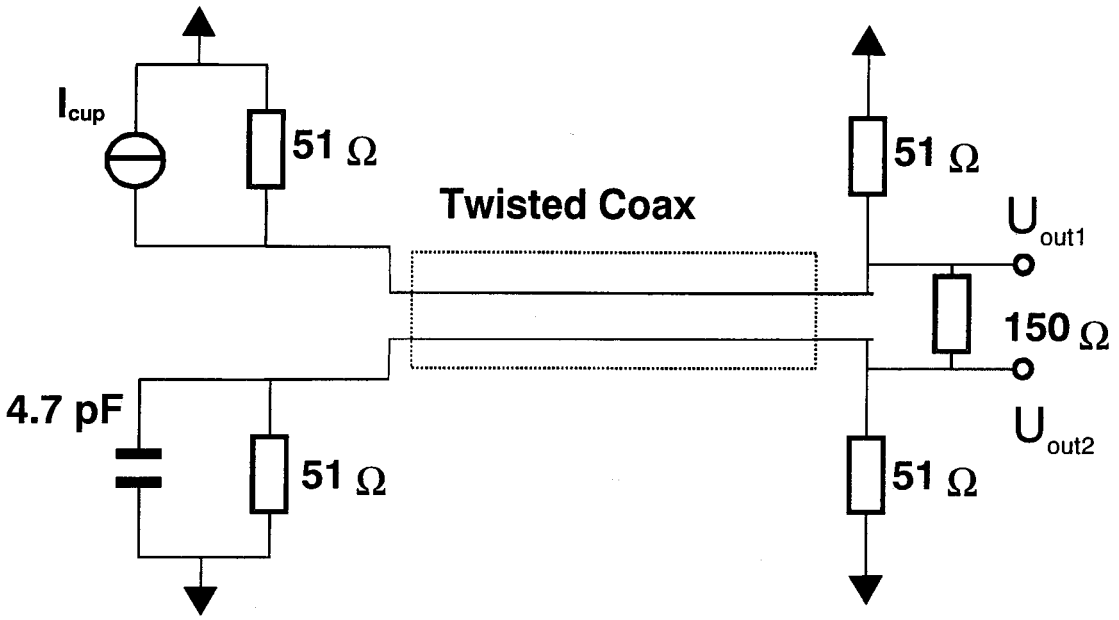

Figure A1 The measurement transmission system for beam measurements.

The impedance of the coax cable is disregarded, because if the impedance at both ends of the cable matches the self-impedance of the cable, the transmission is lossless [KEM95]. Also in further calculations the capacitor, which acts as a dummy Faradaycup is neglected.

From network theory, the so-called Theorem of Theovin, it is known that a current source with a resistor parallel is equivalent to a voltage source with a serial connected resistor, see figure A2.

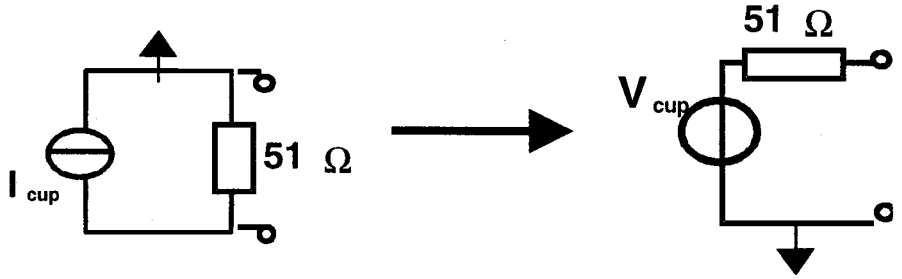

Figure A2 Theorem of Theovin.

If this theorem is used and we replace two paralled placed resistors by one the result is given in figure A3.

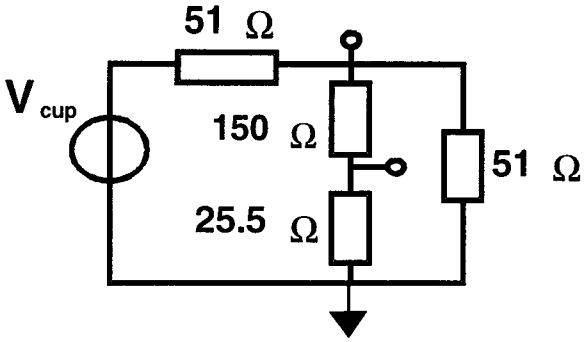

Figure A3 The simplified transmission network, step 1

Figure A3 can be simplified by replacing the two 51 Ω resistors by one resistor. we get the transmission network of figure A4.

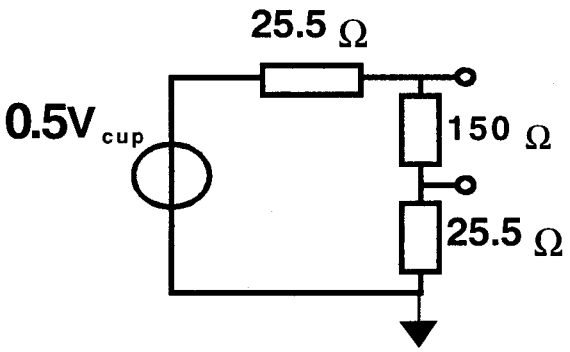

Figure A4 The simplified transmission network

Now we can calculate the resistance as seen by the oscilloscope.

$$V_{oscilloscope} = \frac{150}{150+51} \bullet \frac{1}{2} V_{gun} = 0.37 V_{gun} = 19.0 I_{gun} .$$

Appendix B: Sample input file Parmela

This is the input file used in the longitudinal and tranverse emittance calculations.

```
RUN 1 1 2998.30 0 0.045 7
TITLE
 L10-ALL-withfouriersuperfish
trwave 1.472 1.1 0 0.000 4.46 1 5 2998.30 -1 -5  5 0.666667 1 10
0.00 4.0148 0.1 1.0 60.0
 0.000005  0.000005  0.000009 -0.001105  0.215395  0.985943
-0.004031  0.000013  0.0000013  0.0000013  0.0000013
trwave 1.760 1.1 0 180.000 4.87 1 5 2998.30 -2 -5  5 0.666667 1 10
0.00 3.9844 0.1 1.0 60.0
 0.000005 -0.000001  0.000050 -0.003368  0.279702  0.960024
-0.010480  0.000082 -0.000082  0.000082  0.000082
trwave 2.058 1.1 0 90.000 5.27 1 5 2998.30 -3 -5  5 0.666667 1 10
0.00 3.9621 0.1 1.0 60.0
 0.000005 -0.000007  0.000202 -0.007957  0.334448  0.942149
-0.020884  0.000351 -0.000006  0.000006  0.000006
trwave 2.340 1.1 0 0.000 5.57 1 5 2998.30 -4 -5  5 0.666667 1 10
0.00 3.9461 0.1 1.0 60.0
 0.000002 -0.000025  0.000534 -0.014346  0.367474  0.929330
-0.033208  0.000884 -0.000024  0.000024  0.000024
trwave 2.593 1.1 0 180.000 5.89 1 5 2998.30 -5 -5  5 0.666667 1 10
0.00 3.9347 0.1 1.0 60.0
 0.000004 -0.000060  0.001044 -0.021001  0.379945  0.923572
-0.047017  0.001800 -0.000067  0.000002  0.000002
trwave 2.796 1.1 0 90.000 6.08 1 5 2998.30 -6 -5  5 0.666667 1 10
0.00 3.9271 0.1 1.0 60.0
 0.000009 -0.000114  0.001679 -0.027605  0.392660  0.917456
-0.057625  0.002801 -0.000128  0.000005 -0.000005
trwave 2.965 1.1 0 0.000 6.30 1 5 2998.30 -7 -5  5 0.666667 1 10
0.00 3.9215 0.1 1.0 60.0
 0.000017 -0.000189  0.002460 -0.034742  0.409900  0.909203
-0.064077  0.003630 -0.000187  0.000008 -0.000008
trwave 3.095 1.1 0 180.000 6.42 1 5 2998.30 -8 -5  5 0.666667 1 10
0.00 3.9176 0.1 1.0 60.0
 0.000024 -0.000252  0.002985 -0.038033  0.405742  0.910223
-0.073403  0.004972 -0.000316  0.000020 -0.000001
trwave 3.190 1.1 0 90.000 6.51 1 5 2998.30 -9 -5  5 0.666667 1 10
0.00 3.9150 0.1 1.0 60.0
 0.000031 -0.000315  0.003510 -0.041538  0.409121  0.908161
-0.078058  0.005767 -0.000394  0.000026 -0.000002
trwave 3.262 1.1 0 0.000 6.48 1 5 2998.30 -10 -5  5 0.666667 1 10
0.00 3.9131 0.1 1.0 60.0
 0.000040 -0.000386  0.004105 -0.045893  0.420426  0.902715
-0.078670  0.006040 -0.000423  0.000028 -0.000001
trwave 3.333 1.1 0 180.000 6.60 1 5 2998.30 -11 -5  5 0.666667 1 10
0.00 3.9076 0.1 1.0 60.0
 0.000061 -0.000539  0.005157 -0.050919  0.417233  0.902919
-0.089268  0.008128 -0.000661  0.000052 -0.000003
trwave 3.333 1.0 0 90.000 6.65 1 5 2998.30 -12 -5  5 0.666667 1 10
0.00 3.9005 0.1 1.0 60.0
 0.000079 -0.000667  0.006001 -0.055030  0.420454  0.900727
-0.093587  0.009269 -0.000809  0.000067 -0.000005
trwave 3.333 1.0 0 0.000 6.65 1 5 2998.30 -13 -5  5 0.666667 1 10
```

```
0.00 3.8939 0.1 1.0 60.0
 0.000103 -0.000830  0.007011 -0.059514  0.423861  0.898385
-0.097696  0.010453 -0.000961  0.000081 -0.000005
trwave 3.333 1.0 0 180.000 6.61 1 5 2998.30 -14 -5  5 0.666667 1 10
0.00 3.8907 0.1 1.0 60.0
 0.000103 -0.000830  0.007010 -0.059512  0.423859  0.898386
-0.097694  0.010452 -0.000961  0.000081 -0.000005
trwave 3.333 1.0 0 90.000 6.58 1 5 2998.30 -14 -5  5 0.666667 1 10
0.00 3.8907 0.1 1.0 60.0
trwave 3.333 1.0 0 0.000 6.55 1 5 2998.30 -14 -5  5 0.666667 1 10
0.00 3.8907 0.1 1.0 60.0
trwave 3.333 1.0 0 180.000 6.51 1 5 2998.30 -14 -5  5 0.666667 1 10
0.00 3.8907 0.1 1.0 60.0
trwave 3.333 1.0 0 90.000 6.47 1 5 2998.30 -14 -5  5 0.666667 1 10
0.00 3.8907 0.1 1.0 60.0
trwave 3.333 1.0 0 0.000 6.43 1 5 2998.30 -14 -5  5 0.666667 1 10
0.00 3.8907 0.1 1.0 60.0
trwave 3.333 1.0 0 180.000 6.39 1 5 2998.30 -14 -5  5 0.666667 1 10
0.00 3.8907 0.1 1.0 60.0
trwave 3.333 1.0 0 90.000 6.36 1 5 2998.30 -14 -5  5 0.666667 1 10
0.00 3.8907 0.1 1.0 60.0
trwave 3.333 1.0 0 0.000 6.32 1 5 2998.30 -14 -5  5 0.666667 1 10
0.00 3.8907 0.1 1.0 60.0
trwave 3.333 1.0 0 180.000 6.28 1 5 2998.30 -14 -5  5 0.666667 1 10
0.00 3.8907 0.1 1.0 60.0
trwave 3.333 1.0 0 90.000 6.24 1 5 2998.30 -14 -5  5 0.666667 1 10
0.00 3.8907 0.1 1.0 60.0
trwave 3.333 1.0 0 0.000 6.20 1 5 2998.30 -14 -5  5 0.666667 1 10
0.00 3.8907 0.1 1.0 60.0
trwave 3.333 1.0 0 180.000 6.17 1 5 2998.30 -14 -5  5 0.666667 1 10
0.00 3.8907 0.1 1.0 60.0
trwave 3.333 1.0 0 90.000 6.14 1 5 2998.30 -14 -5  5 0.666667 1 10
0.00 3.8907 0.1 1.0 60.0
trwave 3.333 1.0 0 0.000 6.10 1 5 2998.30 -14 -5  5 0.666667 1 10
0.00 3.8907 0.1 1.0 60.0
trwave 3.333 1.0 0 180.000 6.06 1 5 2998.30 -14 -5  5 0.666667 1 10
0.00 3.8907 0.1 1.0 60.0
trwave 3.333 1.0 0 90.000 6.03 1 5 2998.30 -14 -5  5 0.666667 1 10
0.00 3.8907 0.1 1.0 60.0
trwave 3.333 1.0 0 0.000 6.01 1 5 2998.30 -14 -5  5 0.666667 1 10
0.00 3.8907 0.1 1.0 60.0
trwave 3.333 1.0 0 180.000 5.95 1 5 2998.30 -14 -5  5 0.666667 1 10
0.00 3.8907 0.1 1.0 60.0
trwave 3.333 1.0 0 90.000 5.91 1 5 2998.30 -14 -5  5 0.666667 1 10
0.00 3.8907 0.1 1.0 60.0
trwave 3.333 1.0 0 0.000 5.87 1 5 2998.30 -14 -5  5 0.666667 1 10
0.00 3.8907 0.1 1.0 60.0
trwave 3.333 1.0 0 180.000 5.86 1 5 2998.30 -14 -5  5 0.666667 1 10
0.00 3.8907 0.1 1.0 60.0
trwave 3.333 1.0 0 90.000 5.82 1 5 2998.30 -14 -5  5 0.666667 1 10
0.00 3.8907 0.1 1.0 60.0
trwave 3.333 1.0 0 0.000 5.78 1 5 2998.30 -14 -5  5 0.666667 1 10
0.00 3.8907 0.1 1.0 60.0
trwave 3.333 1.0 0 180.000 5.74 1 5 2998.30 -14 -5  5 0.666667 1 10
0.00 3.8907 0.1 1.0 60.0
trwave 3.333 1.0 0 90.000 5.71 1 5 2998.30 -14 -5  5 0.666667 1 10
0.00 3.8907 0.1 1.0 60.0
trwave 3.333 1.0 0 0.000 5.58 1 5 2998.30 -14 -5  5 0.666667 1 10
0.00 3.8907 0.1 1.0 60.0
trwave 3.333 1.0 0 180.000 5.65 1 5 2998.30 -14 -5  5 0.666667 1 10
```

```
0.00 3.8907 0.1 1.0 60.0
trwave 3.333 1.0 0 90.000 5.61 1 5 2998.30 -14 -5  5 0.666667 1 10
0.00 3.8907 0.1 1.0 60.0
trwave 3.333 1.0 0 0.000 5.57 1 5 2998.30 -14 -5  5 0.666667 1 10
0.00 3.8907 0.1 1.0 60.0
trwave 3.333 1.0 0 180.000 5.55 1 5 2998.30 -14 -5  5 0.666667 1 10
0.00 3.8907 0.1 1.0 60.0
trwave 3.333 1.0 0 90.000 5.51 1 5 2998.30 -14 -5  5 0.666667 1 10
0.00 3.8907 0.1 1.0 60.0
trwave 3.333 1.0 0 0.000 5.48 1 5 2998.30 -14 -5  5 0.666667 1 10
0.00 3.8907 0.1 1.0 60.0
trwave 3.333 1.0 0 180.000 5.46 1 5 2998.30 -14 -5  5 0.666667 1 10
0.00 3.8907 0.1 1.0 60.0
trwave 3.333 1.0 0 90.000 5.41 1 5 2998.30 -14 -5  5 0.666667 1 10
0.00 3.8907 0.1 1.0 60.0
trwave 3.333 1.0 0 0.000 5.39 1 5 2998.30 -14 -5  5 0.666667 1 10
0.00 3.8907 0.1 1.0 60.0
trwave 3.333 1.0 0 180.000 5.34 1 5 2998.30 -14 -5  5 0.666667 1 10
0.00 3.8907 0.1 1.0 60.0
trwave 3.333 1.0 0 90.000 5.32 1 5 2998.30 -14 -5  5 0.666667 1 10
0.00 3.8907 0.1 1.0 60.0
trwave 3.333 1.0 0 0.000 5.30 1 5 2998.30 -14 -5  5 0.666667 1 10
0.00 3.8907 0.1 1.0 60.0
trwave 3.333 1.0 0 180.000 5.26 1 5 2998.30 -14 -5  5 0.666667 1 10
0.00 3.8907 0.1 1.0 60.0
trwave 3.333 1.0 0 90.000 5.22 1 5 2998.30 -14 -5  5 0.666667 1 10
0.00 3.8907 0.1 1.0 60.0
trwave 3.333 1.0 0 0.000 5.18 1 5 2998.30 -14 -5  5 0.666667 1 10
0.00 3.8907 0.1 1.0 60.0
trwave 3.333 1.0 0 180.000 5.15 1 5 2998.30 -14 -5  5 0.666667 1 10
0.00 3.8907 0.1 1.0 60.0
trwave 3.333 1.0 0 90.000 5.12 1 5 2998.30 -14 -5  5 0.666667 1 10
0.00 3.8907 0.1 1.0 60.0
trwave 3.333 1.0 0 0.000 5.11 1 5 2998.30 -14 -5  5 0.666667 1 10
0.00 3.8907 0.1 1.0 60.0
trwave 3.333 1.0 0 180.000 5.06 1 5 2998.30 -14 -5  5 0.666667 1 10
0.00 3.8907 0.1 1.0 60.0
trwave 3.333 1.0 0 90.000 5.05 1 5 2998.30 -14 -5  5 0.666667 1 10
0.00 3.8907 0.1 1.0 60.0
trwave 3.333 1.0 0 0.000 5.01 1 5 2998.30 -14 -5  5 0.666667 1 10
0.00 3.8907 0.1 1.0 60.0
trwave 3.333 1.0 0 180.000 4.955 1 5 2998.30 -14 -5  5 0.666667 1 10
0.00 3.8907 0.1 1.0 60.0
trwave 3.333 1.0 0 90.000 4.95 1 5 2998.30 -14 -5  5 0.666667 1 10
0.00 3.8907 0.1 1.0 60.0
trwave 3.333 1.0 0 0.000 4.93 1 5 2998.30 -14 -5  5 0.666667 1 10
0.00 3.8907 0.1 1.0 60.0
trwave 3.333 1.0 0 180.000 4.89 1 5 2998.30 -14 -5  5 0.666667 1 10
0.00 3.8907 0.1 1.0 60.0
trwave 3.333 1.0 0 90.000 4.86 1 5 2998.30 -14 -5  5 0.666667 1 10
0.00 3.8907 0.1 1.0 60.0
trwave 3.333 1.0 0 0.000 4.84 1 5 2998.30 -14 -5  5 0.666667 1 10
0.00 3.8907 0.1 1.0 60.0
trwave 3.333 1.0 0 180.000 4.80 1 5 2998.30 -14 -5  5 0.666667 1 10
0.00 3.8907 0.1 1.0 60.0
trwave 3.333 1.0 0 90.000 4.77 1 5 2998.30 -14 -5  5 0.666667 1 10
0.00 3.8907 0.1 1.0 60.0
trwave 3.333 1.0 0 0.000 4.72 1 5 2998.30 -14 -5  5 0.666667 1 10
0.00 3.8907 0.1 1.0 60.0
zlimit -20
```

```
coil 3.210 8.5 3730 0 225
coil 5.65 8.5 3730
coil 6.04 8.5 3730
coil 6.50 8.5 3730
coil 6.96 8.5 3730
coil 7.35 8.5 3730
coil 9.79 8.5 3730
coil 12.21 7.7 1657
coil 14.66 7.7 1657
coil 15.26 7.7 1657
coil 15.7 7.7  1657
coil 16.14 7.7 1657
coil 16.74 7.7 1657
coil 19.19 7.7 1657
coil 38.71 7.7 1736
coil 42.41 7.7 1736
coil 45.65 7.7 1736
coil 49.1  7.7 1736
coil 52.55 7.7 1736
coil 55.79 7.7 1736
coil 59.49 7.7 1736
coil 64.81 7.7 1736
coil 68.51 7.7 1736
coil 71.75 7.7 1736
coil 75.2  7.7 1736
coil 78.65 7.7 1736
coil 81.89 7.7 1736
coil 85.59 7.7 1736
coil 94.35  6.86 1514
coil 96.91  6.86 1514
coil 99.04  6.86 1514
coil 101.4  6.86 1514
coil 103.76 6.86 1514
coil 105.89 6.86 1514
coil 108.45 6.86 1514
coil 116.85 6.86 1514
coil 119.41 6.86 1514
coil 121.54 6.86 1514
coil 123.9  6.86 1514
coil 126.26 6.86 1514
coil 128.39 6.86 1514
coil 130.95 6.86 1514
coil 140.02 7.2 1426
coil 143.4  7.2 1426
coil 146.35 7.2 1426
coil 149.5  7.2 1426
coil 152.65 7.2 1426
coil 155.6  7.2 1426
coil 158.98 7.2 1426
coil 164.02 7.2 1426
coil 167.4  7.2 1426
coil 170.35 7.2 1426
coil 173.5  7.2 1426
coil 176.65 7.2 1426
coil 179.6  7.2 1426
coil 182.98 7.2 1426
zout
output 1
INPUT 7 1000 0.0 702.25 1E-4 0.0 702.25 1E-4 360 0.0 0 0
scheff 0.047 0.1 0.1 10 100 0 0 0 0 0
```

```
start 0.0 1.0 9200 20 870
end
```

The RUN card specifies the operation frequency of the accelerating instrument and the initial longitudinal energy of the electrons. In our case 0.045 MeV. The accelerating cells are specified by the TRWAVE cards. They contain the amplitude and the Fouriercoefficients of the longitudinal electric field.

The solenoids of chapter 2 are defined by the COIL cards. Each coil is a single loop coil. Specified by place, radius and current. The INPUT card gives the electron phase-space distribution, in this case a K-V distribution. The SCHEFF card implies the space-charge calculations, with a specified mesh. The START card defines the start phase angle of the reference particle, a phase angle of zero means that the reference particle travels at the crest of the wave. Also the START card specifies the integration parameters, as step size and number of steps.

Appendix C: The Maxwell equations

For completeness of this report the Maxwell equations are also given, since a great part of the described theory is based on them. In context with this report only the differential form in vacuum is given.

The first equation is

$$\nabla \cdot E = 0,$$

the second equation is

$$\nabla \cdot B = 0,$$

the third equation is

$$\nabla \times E = -\frac{\partial}{\partial t} B,$$

and the fourth equation is

$$. \nabla \times B = \mu_0 \varepsilon_0 \frac{\partial}{\partial t} E$$

From these equation the electromagnetic wave equations in vacuum can be derived [POZ93]:

$$\nabla^2 E = \varepsilon_0 \mu_0 \frac{\partial^2 E}{\partial t^2},$$

$$\nabla^2 B = \varepsilon_0 \mu_0 \frac{\partial^2 B}{\partial t^2}.$$